Monthly Notices
of the
ROYAL ASTRONOMICAL SOCIETY

Mon. Not. R. Astron. Soc. **402,** 1081–1098 (2010) doi:10.1111/j.1365-2966.2009.15936.x

The power output of local obscured and unobscured AGN: crossing the absorption barrier with *Swift*/BAT and *IRAS*

R. V. Vasudevan,[1⋆] A. C. Fabian,[1] P. Gandhi,[2] L. M. Winter[3] and R. F. Mushotzky[4]

[1]*Institute of Astronomy, Madingley Road, Cambridge CB3 0HA*
[2]*RIKEN Cosmic Radiation Lab, 2-1 Hirosawa, Wakoshi, Saitama 351-0198, Japan*
[3]*Center for Astrophysics and Space Astronomy, University of Colorado at Boulder, 440 UCB, Boulder, CO 80309-0440, USA*
[4]*Laboratory for High Energy Astrophysics, NASA/GSFC, Greenbelt, MD 20771, USA*

Accepted 2009 October 26. Received 2009 October 6; in original form 2009 July 21

ABSTRACT

The *Swift*/Burst Alert Telescope (BAT) 9-month catalogue of active galactic nuclei (AGN) provides an unbiased census of local supermassive black hole accretion, and probes to all but the highest levels of absorption in AGN. We explore a method for characterizing the bolometric output of both obscured and unobscured AGN by combining the hard X-ray data from the *Swift*/BAT instrument (14–195keV) with the reprocessed infrared (IR) emission as seen with the Infrared Astronomical Satellite (*IRAS*) all-sky surveys. This approach bypasses the complex modifications to the spectral energy distribution introduced by absorption in the optical, UV and 0.1–10 keV regimes and provides a long-term, average picture of the bolometric output of these sources. We broadly follow the approach of Pozzi et al. for calculating the bolometric luminosities by adding nuclear IR and hard X-ray luminosities, and consider different approaches for removing non-nuclear contamination in the large-aperture *IRAS* fluxes. Using mass estimates from the black hole mass-host galaxy bulge luminosity relation, we present the Eddington ratios $\lambda_{\rm Edd}$ and 2–10 keV bolometric corrections for a subsample of 63 AGN (35 obscured and 28 unobscured) from the *Swift*/BAT catalogue, and confirm previous indications of a low Eddington ratio distribution for both samples. Importantly, we find a tendency for low bolometric corrections (typically 10–30) for the obscured AGN in the sample (with a possible rise from $\sim$15 for $\lambda_{\rm Edd} < 0.03$ to $\sim$32 above this), providing a hitherto unseen window on to accretion processes in this class of AGN. This finding is of key importance in calculating the expected local black hole mass density from the X-ray background since it is composed of emission from a significant population of such obscured AGN. Analogous studies with high-resolution IR data and a range of alternative models for the torus emission will form useful future extensions to this work.

Key words: black hole physics – galaxies: active – galaxies: Seyfert.

1 INTRODUCTION

Accretion on to supermassive black holes (SMBHs; with masses of $\sim 10^6$–10^9 solar masses) is responsible for the power output of active galactic nuclei (AGN). Thermal emission from an accretion disc emerges in the optical–UV regime and manifests as the 'Big Blue Bump' (Shields 1978), and inverse Compton scattering of UV disc photons by a corona above the disc is responsible for the X-ray emission (Zdziarski et al. 1990). This optical-to-X-ray emission constitutes the bulk of the intrinsic accretion emission in AGN. In the standard paradigm for AGN, a dusty torus surrounding the accretion disc partially absorbs this emission and re-radiates it in the infrared (IR; Pier & Krolik 1992), manifesting as an IR bump (Elvis et al. 1994). If the AGN is viewed through the torus, the optical-to-X-ray emission may be significantly absorbed along the line of sight, presenting difficulties in determining the true, bolometric accretion luminosity $L_{\rm bol}$ from the central engine. Vasudevan & Fabian (2007) and Vasudevan & Fabian (2009) present $L_{\rm bol}$ (along with bolometric conversion ratios and accretion rates) determined from optical-to-X-ray spectral energy distributions (SEDs) for AGN, but both studies highlight the difficulties associated with determining $L_{\rm bol}$ when spectral complexity associated with absorption is present. In optical surveys of AGN, it is possible for objects to be missed altogether because such absorption can reduce the flux severely enough (reddening) to be below the detection limit.

⋆E-mail: ranjan@ast.cam.ac.uk

Although X-ray surveys are more effective at providing a census of AGN activity (Mushotzky 2004), significant columns of dusty gas (more than $\sim 10^{22}\,\mathrm{cm}^{-2}$) will heavily reduce the X-ray (0.1–10 keV) flux and cause similar problems. Heavily Compton-thick objects (those with column densities $N_{\mathrm{H}} \gg 10^{24}\,\mathrm{cm}^{-2}$) in particular can have X-ray fluxes reduced by many orders of magnitude from their intrinsic flux in this energy band (Ikeda, Awaki & Terashima 2009).

The Burst Alert Telescope (BAT) on board the *Swift* satellite is extremely useful at addressing these considerations to provide a more complete census of AGN activity. The very hard X-ray bandpass of this instrument (14–195 keV) misses absorption signatures for moderate-to-high levels of absorption. The 9-month catalogue of BAT-detected AGN (hereafter the *Swift*/BAT catalogue; Tueller et al. 2008) therefore provides an unprecedented level of completeness when surveying the AGN population, since it contains all but the most heavily absorbed objects. The X-ray properties of the 153 AGN in the catalogue are presented in Winter et al. (2009), using data from a variety of X-ray missions to determine their intrinsic luminosities, spectral shapes (including measures of the spectral complexity) and absorbing column densities (N_{H}). Vasudevan et al. (2009) present simultaneous optical-to-X-ray SEDs from *Swift*'s X-ray telescope (XRT) and UV–optical telescope (UVOT) and calculate the total accretion output L_{bol} and associated quantities for a subsample of 26 local, low-absorption, low-spectral-complexity AGN from the *Swift*/BAT catalogue. For their subsample of objects, the aforementioned problems associated with absorption are minimized or straightforwardly corrected for. Their work provides hints that the local AGN population is dominated by AGN in which X-ray emission processes contribute significantly to the bolometric emission, manifesting as low bolometric corrections $\kappa_{2-10\mathrm{keV}}$ ($\kappa_{2-10\mathrm{keV}} = L_{\mathrm{bol}}/L_{2-10\mathrm{keV}} \sim 10$–$30$ for 2–10 keV luminosity $L_{2-10\mathrm{keV}}$), and also suggests that accretion rates are low (Eddington ratios $\lambda_{\mathrm{Edd}} \lesssim 0.1$, where $\lambda_{\mathrm{Edd}} = L_{\mathrm{bol}}/L_{\mathrm{Edd}}$ for Eddington luminosity $L_{\mathrm{Edd}} = 1.3 \times 10^{38}(M_{\mathrm{BH}}/\mathrm{M}_{\odot})$ for a black hole of mass M_{BH}). While such an approach is of particular utility for determining the total power output of unobscured AGN, an alternative approach is needed to address this question more generally for AGN of all absorption levels. This study explores a method for crossing the 'absorption barrier', and aims to characterize the bolometric output of local AGN in the *Swift*/BAT 9-month catalogue sources across the range of absorption properties probed by the catalogue.

The hard X-ray data from the BAT instrument gathered over many months are available for the *Swift*/BAT catalogue sources and are presented online. These data provide a useful starting point for our absorption-unbiased study on the bolometric AGN power output. However, instead of using optical–UV emission to constrain the thermal emission from the accretion disc, we use the reprocessed IR emission to estimate the non-X-ray component of the bolometric luminosity L_{bol}. We take the reprocessed IR emission to be a severely averaged proxy for the intrinsic disc emission, since the time-scale for transferral of energy from the high-energy flux at the inner edge of the torus to emission as IR at its outer edge is of the order of several years in standard models (Barvainis 1987); whereas optical, UV and X-ray variability in AGN is known to occur on far shorter time-scales (a few minutes to hours). The averaged accretion output represented by the IR can be used in conjunction with the long-term hard X-ray observations to estimate L_{bol}. We use the archival mid-to-far-IR observations from the Infrared Astronomical Satellite (*IRAS*) all-sky catalogues to measure this reprocessed output; mid-IR (MIR) observations in particular are well suited to our purposes since they capture the emission in the range where reprocessed AGN emission is expected to peak ($\sim$12 μm) and the all-sky surveys readily available in the archives are ideal for identifying IR counterparts to X-ray sources in the all-sky *Swift*/BAT catalogue. Our method is a low-redshift, absorption-'neutral' extension of the work of Pozzi et al. (2007) on high-redshift luminous obscured quasars, with the key difference being the use of hard X-ray BAT data instead of 2–10 keV X-ray data.

When considering the effects of absorption in AGN, it is important to note that the absorbing columns measured in different wavebands do not always match. Under the standard unified scheme for AGN discussed above, one would expect an AGN with significant X-ray gas absorption to exhibit significant dust absorption in the optical–UV (if one assumes a relatively constant dust-to-gas ratio across the AGN population). However, there are many classes of object which do not obey this simple picture, as discussed by Maiolino & Risaliti (2007). However, statistically speaking, X-ray and optical absorptions are broadly correlated, and significant mismatch occurs in only about 10–20 per cent of the AGN populations studied in various surveys (e.g. Garcet et al. 2007; Mateos et al. 2005; Silverman et al. 2005). In any case, these considerations do not significantly affect the approach used here, but we return to this issue when calculating the reprocessed IR emission. In this paper, whenever the labels 'absorbed/obscured' or 'unabsorbed/unobscured' are used, they consistently refer to X-ray absorption.

The use of the IR emission as an indication of AGN activity is supported by numerous works. Mushotzky et al. (2008) find a strong correlation between the hard X-ray BAT luminosity and the Two-Micron All-Sky Survey (2MASS) *J*-band luminosity. McKernan et al. (2009) use analyses of X-ray observations from the literature and *IRAS* data to calculate X-ray-to-IR luminosity ratios, and identify from these that the parameters specifying the physical AGN environment such as the torus geometry must span a narrow range. The study of Gandhi et al. (2009) discusses the correlation between X-ray (2–10 keV) emission and IR emission in detail for a sample of Seyfert nuclei, again using X-ray analyses from the literature and new IR data from the Very Large Telescope's Imager and Spectrometer for MIR (VISIR/VLT), taken specifically for addressing the issue of nuclear emission in local Seyferts. Their data are the best estimates of the nuclear (non-stellar) IR flux in AGN to date, and show a strong correlation between intrinsic, uncontaminated nuclear IR monochromatic luminosity (at 12.3 μm) and 2–10 keV X-ray luminosity. Their work reinforces the idea that the uncontaminated MIR continuum is an accurate proxy for the intrinsic power of AGN, and reinforces and improves constraints on previous determinations of the correlation (Horst et al. 2008, 2006). They also highlight the usefulness of extending this approach to a very hard X-ray selected sample such as the one used here. Their correlation also provides one way to estimate non-nuclear contamination in IR observations taken with larger apertures, as is the case with the *IRAS* data used here. The other method employed for correcting for non-nuclear contamination in this study is fitting of host galaxy and nuclear SED templates to the mid-to-far IR SEDs.

In this paper, we use the *IRAS* and BAT data to generate SEDs from which the reprocessed IR and intrinsic X-ray emission can be determined, for calculation of L_{bol}. We calibrate this approach against integration of the optical-to-X-ray SEDs as presented in Vasudevan et al. (2009), using the sources overlapping between the two studies for this purpose. We note that although our *IRAS* and BAT data are not contemporaneous, they both represent an averaged, long-term picture of accretion whereas the simultaneous optical-to-X-ray data presented in Vasudevan et al. (2009) are a 'snapshot' of the accretion emission at a particular time. That approach has

numerous advantages (as discussed in Vasudevan & Fabian 2009), but the average, long-term picture should be found to agree with 'snapshots' when considering a reasonably large sample of objects, since the effects of variability should be averaged out over many sources. Certainly, 'quasi-simultaneous' data between hard X-ray and IR are preferable since ideally we want the IR to capture a reprocessed version of the same long-term state seen at higher energies, but the IR and hard X-ray bands can afford to be separated by much longer time periods to qualify as 'quasi-simultaneous' due to the large time-scales involved in reprocessing. We present the bolometric luminosities, Eddington ratios and bolometric corrections determined for all the local ($z < 0.1$) objects in the *Swift*/BAT catalogue with good quality *IRAS* and BAT data, using black hole mass estimates calculated from *K*-band host bulge luminosity estimates via the method of Vasudevan et al. (2009) to determine accretion rates (apart from for Cyg A, where a known dynamical mass estimate is used).

This study can offer perspectives on unification schemes for AGN (Antonucci 1993), as it provides an idea of which type of accretion processes dominate in AGN (as parametrized by the X-ray bolometric correction) over a range of absorbing column densities and hence orientations. A flat Universe ($\Omega_M + \Omega_\Lambda = 1$) with a cosmology $H_0 = 71\,\mathrm{km\,s^{-1}\,Mpc^{-1}}$ and $\Omega_\mathrm{M} = 0.27$ has been assumed throughout this work.

2 SAMPLE SELECTION

We firstly apply a redshift cut ($z < 0.1$) on the 145 sources with spectral properties presented in Winter et al. (2009) and exclude sources which would exhibit prominent jet contributions to their luminosity such as BL Lacs or blazars (see Winter et al. 2009), yielding 116 potential objects. We then exclude the two merging galaxies NGC 6921 and MCG +04-48-002 since AGN at such close proximity are very likely to be confused in the low-resolution *IRAS* images. We also exclude the galaxy NGC 6814 which is known to have a prominent cataclysmic variable in the foreground, yielding 113 potential objects.

In assembling *IRAS* data for this sample, we take care to ensure confident positional matches between the *IRAS* catalogues and the NASA Extragalactic Database (NED) positions. We preferentially use the *IRAS* Point Source Catalogue (PSC) as our source for IR photometry; if data were not available in this catalogue we then turned to the *IRAS* Faint Source Catalogue (FSC), which also catalogues point sources. There was some overlap between the PSC and FSC; in many cases, the FSC provided greater wavelength coverage and data quality than the PSC. The 12, 25, 60 and 100 μm photometry for these catalogues are available online[1] along with useful diagnostic and data quality information. The positional accuracy of the *IRAS* photometry is dependent on a number of factors. We first of all restrict our searches to within 180 arcsec of the NED positions of our AGN (bearing in mind the PSF full width at half-maximum of ∼1−5 arcmin for *IRAS*), yielding 70 matches in the PSC and 73 matches in the FSC (with significant overlap between the two). We then employ the information on the positional error ellipses for the *IRAS* photometry provided for each object, to gauge the goodness of the positional match. The semimajor and semiminor axes (σ_maj, σ_min) for each error ellipse are provided (in arcsec), and we determine an error circle of radius $\sigma_\mathrm{pos} = (\sigma_\mathrm{maj}\sigma_\mathrm{min})^{1/2}$ with the same area as the ellipse defined by these axes. We require the *IRAS* photometry to have a position within $3\sigma_\mathrm{pos}$ of the NED position, taking care to ensure that only one *IRAS* source matched for each object to avoid confusion with other sources in the field. For the purposes of probing the nuclear emission, we require that there are *IRAS* data available at least one of 12 or 25 μm (both are preferred, to get an impression of the shape of the IR AGN SED).

We then enforce a quality criterion on the *IRAS* photometry, requiring at least one of the 12–100 μm points to have a signal-to-noise ratio (SNR) greater than 4.0, and not using any data with an SNR < 3.0. The photometry satisfying the above stringent criteria was used in further analyses. This yielded 71 out of 113 objects in the low-redshift sample. We identify the sources for which processed 9-month BAT data are available online[2] (see Tueller et al. 2008). We also require that an estimate of the black hole mass from the 2MASS PSC magnitudes is available, using the method presented in Vasudevan et al. (2009). The 2MASS magnitude for the cD galaxy Cyg A yields a very low estimate of the black hole mass ($\log M_\mathrm{BH}/\mathrm{M}_\odot = 7.9$), since the bulge is unusually large in this particular galaxy. We therefore use the more reliable dynamical mass estimate from Tadhunter et al. (2003) for this object ($\log M_\mathrm{BH}/\mathrm{M}_\odot = 9.4$). This finally yields 64 objects for further analysis, listed in Table 1 (29 low-absorption and 35 high-absorption objects), constituting 57 per cent of the available low-redshift sample. Luminosity distances are computed from redshifts for most of the sample. Due to the large number of NGC galaxies in the sample, we use the redshift-independent distance estimates from the Nearby Galaxies Catalogue where available (Tully 1994) and scale luminosities appropriately. This only produces a pronounced change for two objects, NGC 4388 (where the change in luminosity from the redshift-estimated distance is a factor of ∼4) and NGC 4051 (where the luminosity changes by a factor of ∼3). For all other NGC galaxies, the changes are negligible and less than the random errors from other sources. To allow easy comparison with previous work in this area and on the 9-month catalogue, we finally bifurcate the sample on N_H, producing two subsamples of low ($\log N_\mathrm{H} < 22$, 51 AGN) and high ($\log N_\mathrm{H} > 22$, 61 AGN) absorption (using the dividing line between 'obscured' and 'unobscured' sources suggested by Winter et al. 2009).

3 GENERATING SEDS FROM BAT AND *IRAS* DATA

3.1 BAT data

The four-channel BAT data are available readily processed online (see Section 2) for analysis with the X-ray analysis software XSPEC. The key goal of using the BAT data is to obtain an accurate estimate of the intrinsic X-ray continuum. The BAT data become particularly useful at determining the intrinsic spectral shape and normalization in the more obscured sources (provided they are not too Compton thick, $N_\mathrm{H} \gg 10^{24}\,\mathrm{cm^{-2}}$).

For our purposes, we wish to extrapolate the 2–10 keV luminosities of these sources from their BAT data in order to calculate bolometric corrections. These luminosities also allow comparison with the $L_{12.3\,\mu\mathrm{m}}$–$L_{2-10\,\mathrm{keV}}$ correlation presented in Gandhi et al. (2009). The key assumption needed when extrapolating to calculate $L_{2-10\,\mathrm{keV}}$ is the spectral shape across the X-ray continuum, parametrized by the photon index Γ, assuming an intrinsic spectrum consisting of a power law of the form $N(E) \propto E^{-\Gamma}$ across the

[1] http://irsa.ipac.caltech.edu/applications/Gator/

[2] http://swift.gsfc.nasa.gov/docs/swift/results/bs9mon/

Table 1. Objects used in the sample.

AGN	$N_{\rm H}/(10^{22}\,{\rm cm}^{-2})$	Redshift	Comments
3C 382	–	0.05787	Radio galaxy
ESO 548−G081	–	0.01448	
Mrk 590	–	0.026 385	
Mrk 766	–	0.012 929	
Mrk 841	–	0.036 422	
NGC 4051	–	0.002 336	
NGC 7469	–	0.016 317	
NGC 985	–	0.043 143	
IRAS 05589+2828	$0.00^{+0.04}$	0.033	
Mrk 79	0.0063 (upper limit)	0.022 189	
Mrk 279	0.013 (upper limit)	0.030 451	
Mrk 509	$0.015^{+0.008}_{-0.008}$	0.034 397	
NGC 7213	$0.025^{+0.011}_{-0.012}$	0.005 839	
NGC 4593	$0.031^{+0.011}_{-0.012}$	0.009	
2MASX J21140128+8204483	$0.047^{+0.023}_{-0.021}$	0.084	Radio galaxy
NGC 5548	$0.07^{+0.04}_{-0.05}$	0.017 175	
ESO 511−G030	$0.098^{+0.021}_{-0.021}$	0.022 389	
3C 390.3	$0.12^{+0.03}_{-0.03}$	0.0561	Radio galaxy
Mrk 290	$0.15^{+0.03}_{-0.05}$	0.029 577	
3C 120	$0.16^{+0.01}_{-0.01}$	0.03301	Radio galaxy
MCG −06-30-015	$0.19^{+0.03}_{-0.01}$	0.007 749	
MCG +08-11-011	$0.25^{+0.016}_{-0.015}$	0.020 484	
ESO 490-G026	$0.33^{+0.04}_{-0.02}$	0.02485	
NGC 3516	$0.353^{+0.32}_{-0.12}$	0.008 836	
NGC 931	$0.36^{+0.08}_{-0.08}$	0.016 652	
NGC 3783	$0.57^{+0.21}_{-0.14}$	0.009 73	
IC 4329A	$0.61^{+0.03}_{-0.03}$	0.016 054	
NGC 4945	$0.793^{+0.957*}_{-0.495}$	0.001 878	
IRAS 09149-6206	$0.85^{+0.26}_{-0.17}$	0.0573	
NGC 7314	$1.16^{+0.01}_{-0.14}$	0.004 763	
NGC 2992	$1.19^{+2.21}_{-0.96}$	0.007 71	
Mrk 3	$1.24^{+5.67}_{-1.24}$	0.013 509	
4U 1344-60	$1.45^{+0.20}_{-0.19}$	0.012 879	
NGC 526A	$1.50^{+0.14}_{-0.14}$	0.019 097	
NGC 3227	$1.74^{+0.12}_{-0.09}$	0.003 859	
EXO 055620−3820.2	$2.57^{+0.14}_{-0.14}$	0.033 87	
NGC 5506	$2.78^{+0.05}_{-0.05}$	0.006 181	
NGC 2110	$2.84^{+0.19}_{-0.16}$	0.007 789	
Mrk 6	$3.26^{+1.33}_{-1.19}$	0.018 813	
2MASX J04440903+2813003	$3.39^{+0.31}_{-0.25}$	0.011 268	
NGC 6860	$4.53^{+1.33}_{-1.30}$	0.014 884	
ESO 005-G004	$5.58^{+0.16}_{-0.16}$	0.006 228	
NGC 7582	$7.39^{+1.46}_{-1.00}$	0.005 254	
NGC 7172	$8.19^{+3.42}_{-3.30}$	0.008 683	
Cyg A	$11.0^{+21.0}_{-6.0}$	0.056 075	cD galaxy, radio galaxy
PGC 13946	$14.4^{+7.4}_{-5.9}$	0.036 492	
Mrk 348	16^{+4}_{-3}	0.015 034	
Mrk 1498	$17.84^{+2.37}_{-1.82}$	0.0547	
Mrk 18	$18.25^{+3.64}_{-2.71}$	0.011 088	
NGC 6300	$21.5^{+0.8}_{-0.9}$	0.003 699	
ESO 103-035	$21.6^{+2.6}_{-2.5}$	0.013 286	
IC 5063	$21.78^{+2.24}_{-2.06}$	0.011 348	
NGC 4507	$34.28^{+4.50}_{-4.57}$	0.011 801	

Table 1 – *continued*

AGN	$N_{\rm H}/(10^{22}\,{\rm cm}^{-2})$	Redshift	Comments
NGC 4388	$36.17^{+3.81}_{-3.82}$	0.008 419	
MCG −03-34-064	$40.73^{+4.79}_{-4.30}$	0.016 541	
ESO 297−018	$41.71^{+4.70}_{-2.90}$	0.0252	
3C 403	$45.0^{+7.0}_{-6.0}$	0.059	Radio galaxy
NGC 788	$46.89^{+4.68}_{-4.47}$	0.013 603	
ESO 506−G027	$76.82^{+7.37}_{-6.79}$	0.025 024	
NGC 1142	$79.75^{+5.81}_{-3.05}$	0.028 847	
NGC 5728	$82.0^{+5.3}_{-5.0}$	0.009 353	
NGC 3281	$86.3^{+16.32}_{-16.12}$	0.010 674	
NGC 1365	104.8	0.005 457	
NGC 612	$129.70^{+12.90}_{-8.30}$	0.029 771	Radio galaxy

Note. Values of absorbing column density $N_{\rm H}$ are taken from Winter et al. (2009). *For NGC 4945, observations spanning 2–20 keV from the *Ginga* satellite (Iwasawa et al. 1993) yield a much higher value for $N_{\rm H}$ of $10^{24.7}\,{\rm cm}^{-2}$, placing it in the heavily 'obscured' category; the optical images reveal a heavily dust-extincted edge-on galaxy.

whole 0.1–200 keV range. The analysis of Tueller et al. (2008) suggests an average photon index of ∼2 in the BAT energy band with an rms spread of ∼0.3. We first consider the approach of calculating the intrinsic 2–10 keV luminosities by employing $\Gamma = 2$ for all sources, but this yields systematically higher values of $L_{2-10\,{\rm keV}}$ than those from X-ray analyses presented in Winter et al. (2009). Although the BAT 9-month data are averaged over many months and the X-ray analyses in Winter et al. (2009) are from individual shorter observations, statistically one expects better agreement, assuming the X-ray analyses have managed to recover the true intrinsic luminosity.

A second approach involves using the values of the 2–10 keV photon indices presented in Winter et al. (2009) to constrain the *shape* of the overall X-ray spectrum, but using the BAT data to constrain the *normalization* and hence the luminosity. The X-ray variability seen in the well-studied type 1 Seyfert galaxy MCG −06-30-15 supports such an approach, as the observations are consistent with variation in normalization while maintaining a relatively constant spectral shape (Vaughan & Fabian 2004; Miniutti et al. 2007). This produces better agreement and less of a systematic shift above the Winter et al. (2009) values, but still results in a large scatter. Part of this could be attributable to extreme values of Γ found for some of these sources in the X-ray analyses. On physical grounds, one expects a minimal photon index of ∼1.5 on canonical inverse-Comptonization scattering models for the coronal emission, and similarly photon indices above ∼2.2 are likely to indicate complex absorption is preventing the recovery of the intrinsic shape, despite the inclusion of some absorption components. In our final approach, we therefore constrain Γ to lie within the hard limits $1.5 < \Gamma < 2.2$ when the values from Winter et al. (2009) lie outside this range. This correction is seen to be necessary for a number of the high-absorption, 'complex' spectrum sources identified in Winter et al. (2009). The scatter between the BAT values and the Winter et al. values is significantly reduced, and the results of this comparison are presented in Fig. 1. We note that there are two objects which deviate significantly from the one-to-one correspondence line: these are NGC 4945 at $\log(L^{\rm (Winter)}_{2-10\,{\rm keV}}) \sim 40.1$ (classified as unobscured in Winter et al. 2009) and 3C 403 at $\log(L^{\rm (Winter)}_{2-10\,{\rm keV}}) \sim 42.8$ (classified as obscured). Despite the identification of the former as unobscured in Winter et al. (2009), both of these are known to have very complex spectra in which the 2–10 keV luminosity is prone to being under-

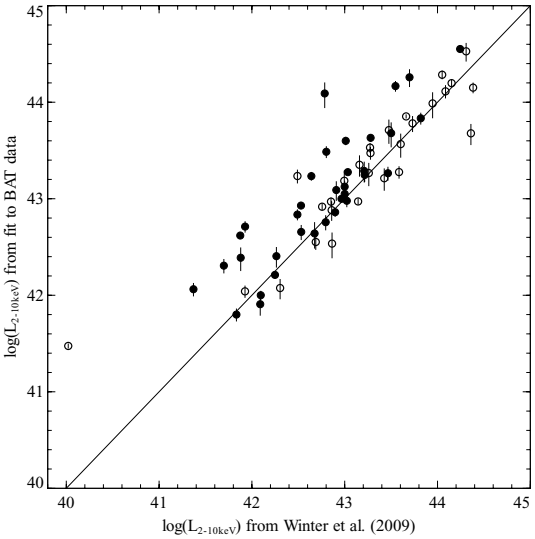

Figure 1. Comparison between 2–10 keV X-ray luminosity extrapolated from fitting to the BAT data with the values presented in Winter et al. (2009). The photon indices (Γ) from Winter et al. (2009) were used in fitting the BAT data, but were restricted to lie within $1.5 < \Gamma < 2.2$ on physical grounds. Filled circles and empty circles represent objects with high and low absorption, respectively [with objects above $\log(N_{\rm H}) = 22$ classed as having high absorption].

estimated with simple absorbed power-law fits (see e.g. Iwasawa et al. 1993). The BAT-extrapolated values for $L_{2-10\,{\rm keV}}$ are likely to be more representative in these cases.

Having thus determined a sensible X-ray spectrum, we determine the total X-ray luminosity by integrating between 0.5 and 100 keV. A cut-off of 500 keV (as used by Pozzi et al. 2007) would not produce an appreciable difference in total X-ray luminosities for objects with $\Gamma \sim 2$. The effect would be ∼20 per cent in the X-ray luminosity, but since the dominant component of $L_{\rm bol}$ is the accretion disc emission (reprocessed or otherwise) this choice of cut-off does not have a big impact. Additionally, a 500 keV cut would be outside the BAT bandpass. Recent work by Mushotzky et al. (in preparation) suggests that the majority of high-energy

cut-offs in BAT spectra for the 22-month catalogue AGN are located at ∼100 keV, which would support the use of the upper integration limit energy used here.

We note that two objects in our high-absorption sample could be borderline Compton thick ($N_{\rm H} > 10^{24}$ cm^{-2}) in Winter et al. (2009), namely NGC 612 and NGC 1365. In the case of NGC 1365, this source has been identified to have variable absorption, with the source switching between Compton-thick and Compton-thin states on time-scales of a few tens of kiloseconds (Risaliti et al. 2009). There are additionally some sources which are identified as Compton thick in the literature due to different approaches of modelling the spectrum (e.g. Mrk 3, Awaki et al. 2008, NGC 4945, Iwasawa et al. 1993). The galaxy NGC 4945 in particular may have $N_{\rm H}$ as high as $10^{24.7}$ cm^{-2} (Iwasawa et al. 1993), making it unsuitable for the type of $L_{\rm bol}$ calculation used here, and we therefore exclude it from our final bolometric correction results. The other very high-absorption objects represent the limits of the approach outlined here and their results must be treated with caution.

3.2 *IRAS* data

The next step in the process is to determine the total nuclear IR luminosity, which, under the reprocessing paradigm, constitutes the remaining major component of the bolometric luminosity. The *IRAS* 12 and 25 μm fluxes are thought to be dominated by the nuclear component, but they are typically calculated for apertures significantly larger than the expected torus dimensions – indeed for the vast majority of local AGN the torus cannot be resolved even with very high-resolution imaging. There is therefore a likelihood of significant non-nuclear flux contaminating the photometry, which we now turn to address.

3.2.1 Host galaxy/starburst contamination in IRAS fluxes (1): using the $L_{12\,\mu\rm m}$–$L_{2-10\,\rm keV}$ relation

Gandhi et al. (2009) present a strong correlation between nuclear 12.3 μm and 2–10 keV luminosities for AGN. Assuming the colour correction between 12 and 12.3 μm is negligible, we can compare the relationship between our *IRAS* 12 μm luminosity and BAT-derived 2–10 keV luminosity with that from Gandhi et al. (2009), to get a statistical estimate of the degree of host galaxy contamination present in the *IRAS* fluxes at different X-ray luminosities. We present these data in Fig. 2, in addition to the correlation found for well-resolved sources from Gandhi et al. (2009). This comparison also assumes that the flux discrepancies introduced by the different filters on *IRAS* and the VLT are negligible (the broad *IRAS* 12 μm filter could include many features contaminating the continuum, whereas the much narrower 12.3 μm VLT filter is likely to provide a better sample of the continuum).

It is clear that the non-nuclear excess in the 12-μm luminosity increases with lower X-ray luminosity; this is expected since at lower intrinsic nuclear luminosities (as traced by $L_{2-10\rm keV}$), it is more difficult for the nucleus to outshine the host galaxy. This excess is likely to be due to star-formation. We determine the excess with respect to the Gandhi et al. (2009) relation for all the AGN with detections in *IRAS* and plot them against $L_{2-10\,\rm keV}$ in Fig. 3. We also include upper limits for 39 AGN without *IRAS* detections, taking care to check whether the objects in this list were in a part of the sky surveyed by *IRAS*. We take the completeness limit of the *IRAS* FSC to be the upper limiting flux for these objects, ∼0.2 Jy.[3]

We use the *Astronomy Survival Analysis* (ASURV) package from the StatCodes suite of utilities developed by Eric Feigelson[4] to determine the correlation between the excess $\Delta\log(L_{12\,\mu\rm m})$ and $\log L_{2-10\,\rm keV}$ including the effects of the upper limits. The 'EM'

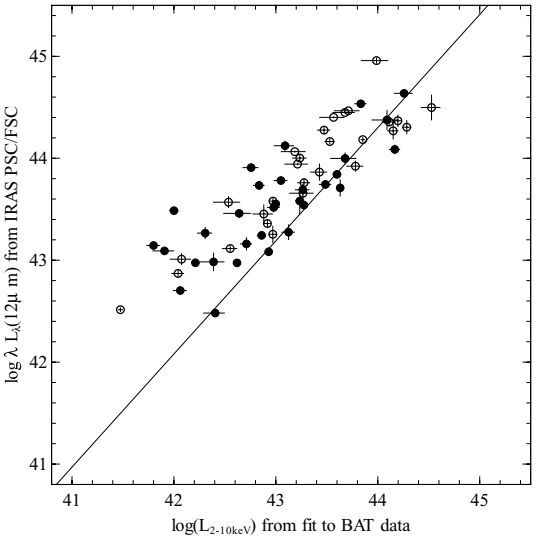

Figure 2. IR 12 μm luminosity against 2–10 keV luminosity from fits to BAT data. The solid line represents the correlation found for well-resolved sources from Gandhi et al. (2009). Filled circles and empty circles represent objects with high and low absorption, respectively [with objects above $\log(N_{\rm H}) = 22$ classed as having high absorption].

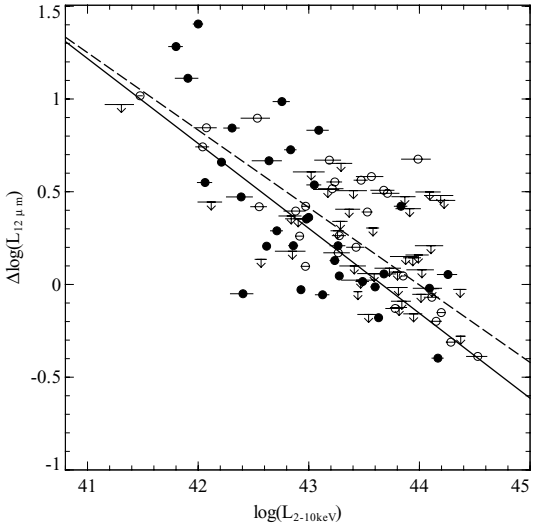

Figure 3. Offset $\Delta\log L_{12\,\mu\rm m}$ between *IRAS* 12 μm fluxes and the relation of Gandhi et al. (2009), plotted against $L_{2-10\,\rm keV}$. Detected objects are represented using black filled circles (obscured objects) and empty circles (unobscured objects), and upper limits are shown using downward pointing arrows. The solid line is the best fit taking upper limits into account (using the EM algorithm in the ASURV utility), and the dashed line shows the fit from ignoring non-detections. Over the luminosity range of the sample, the differences are not significant.

[3] http://irsa.ipac.caltech.edu/IRASdocs/surveys/fsc.html
[4] http://astrostatistics.psu.edu/statcodes/sc_censor.html

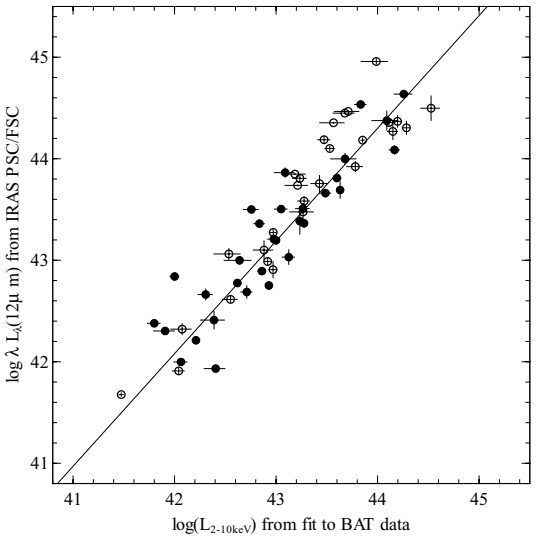

Figure 4. IR 12 μm luminosity against 2–10 keV luminosity from fits to BAT data, corrected for the excess starburst/host galaxy flux seen in the large apertures for *IRAS*. The excess host contribution was obtained by comparing the correlation from our data with that from Gandhi et al. (2009).

and 'Buckley–James' algorithms available in ASURV yield almost identical results. We obtain the following non-nuclear 12 μm excess:

$$\Delta\log(\mathrm{L}_{12\,\mu\mathrm{m}}) = 19.988 - 0.4578\log(\mathrm{L}_{2-10\,\mathrm{keV}}). \quad (1)$$

The correction exhibits a significant dependence on luminosity: for AGN with $\log(L_{2-10\,\mathrm{keV}}) \sim 41$, the total IR 12 μm flux is estimated to be ∼20 times larger than the nuclear flux alone, reducing to zero at X-ray luminosities of $\log(L_{2-10\,\mathrm{keV}}) \sim 43.5$. We then correct the 12 μm luminosities according to this correction (up until the threshold at which the correction becomes negative) and replot the results in Fig. 4.

In this approach, we assume that the 25 μm luminosity needs to be corrected by the same factor, despite a possible larger non-nuclear contribution at longer wavelengths. The larger excess expected at 25 μm would further decrease the total IR nuclear luminosities obtained. However, since we do not have any information on the 25 μm–$L_{2-10\,\mathrm{keV}}$ correlation, an estimation of the extra correction required is beyond the scope of this paper.

The $L_{12\,\mu\mathrm{m}}-L_{2-10\mathrm{keV}}$ correlation in Seyferts itself presents a possibility for predicting the approximate range of bolometric corrections under the reprocessing paradigm, since the $L_{12\,\mu\mathrm{m}}-L_{2-10\mathrm{keV}}$ relation links the two bands used in our calculation of L_{bol}.

We take the bolometric luminosity L_{bol} to be the sum of the total integrated IR luminosity and the total X-ray luminosity, i.e. $L_{\mathrm{bol}} = L_{\mathrm{IR,tot}} + L_{\mathrm{X,tot}}$. Assuming that the monochromatic 12 μm luminosity scales up to the total integrated luminosity by some factor K, dependent on the IR SED and including the effects of geometry and anisotropy (see Section 3.2.3 for details), we can rewrite this as

$$L_{\mathrm{bol}} = K L_{12\,\mu\mathrm{m}} + L_{\mathrm{X,tot}}. \quad (2)$$

This can be converted into an expression for the bolometric correction $\kappa_{2-10\,\mathrm{keV}}$ by dividing through by $L_{2-10\,\mathrm{keV}}$:

$$\kappa_{2-10\mathrm{keV}} = K\,\frac{L_{12\,\mu\mathrm{m}}}{L_{2-10\,\mathrm{keV}}} + \frac{L_{\mathrm{X,tot}}}{L_{2-10\mathrm{keV}}}. \quad (3)$$

The final part of the expression $L_{\mathrm{X,tot}}/L_{2-10\,\mathrm{keV}}$ is constrained to lie within 3.1 and 5.3 by the range of photon indices $1.5 < \Gamma < 2.2$ adopted here as discussed in Section 3.1. We can then include the $L_{12\,\mu\mathrm{m}}-L_{2-10\,\mathrm{keV}}$ relation as $L_{12\,\mu\mathrm{m}} = 10^a L^b{}_{2-10\,\mathrm{keV}}$ to finally obtain

$$\kappa_{2-10\mathrm{keV}} = K\,10^a L^{(b-1)}_{2-10\,\mathrm{keV}} + \frac{L_{\mathrm{X,tot}}}{L_{2-10\mathrm{keV}}}. \quad (4)$$

The distribution of bolometric corrections seen will therefore depend on the diversity of IR SED shapes and assumptions about torus geometry and emission (via K), the degree of spread intrinsic to the measured $L_{12\,\mu\mathrm{m}}-L_{2-10\,\mathrm{keV}}$ relation (via a and b) and the amount of variation in the X-ray spectral shape (via $L_{\mathrm{X,tot}}/L_{2-10\,\mathrm{keV}}$). The nuclear SED templates from Silva, Maiolino & Granato (2004) used in this paper, in conjunction with assumptions about torus geometry and anisotropy of emission (Section 3.2.3), yield a range in K of 4−15. Combining this with the spread in a and b reported in Gandhi et al. (2009) and the range of X-ray SED shapes discussed above, this predicts bolometric corrections ranging from 6 to 60 over the luminosity range $41.0 < \log(L_{2-10\mathrm{keV}}) < 45.0$ spanned by the objects considered here, with an increase in $\kappa_{2-10\,\mathrm{keV}}$ with $L_{2-10\,\mathrm{keV}}$ as predicted by equation (4). Therefore, by requiring that our objects lie on the $L_{12\,\mu\mathrm{m}}-L_{2-10\,\mathrm{keV}}$ relation, we naturally expect a certain distribution of bolometric corrections, with the degree of spread related to the tightness of the $L_{12\,\mu\mathrm{m}}-L_{2-10\,\mathrm{keV}}$ relation observed. The tighter the distribution the smaller the range of bolometric corrections will be, centring around 10–30. Since, under the assumptions used in our paper, the requirement of a tight $L_{12\,\mu\mathrm{m}}-L_{2-10\,\mathrm{keV}}$ relation can limit the range of bolometric corrections allowed, we also consider an approach for removal of the non-nuclear component which is independent of the $L_{12\,\mu\mathrm{m}}-L_{2-10\,\mathrm{keV}}$ relation.

3.2.2 Host galaxy/starburst contamination in IRAS fluxes (2): using host galaxy IR SED templates

We also employ the strategy used by Pozzi et al. (2007) to account for the host galaxy, namely fitting the nuclear and host galaxy SED templates from Silva et al. (2004) to the broad-band (12–100 μm) IR data. This does not presuppose any relation between L_{IR} and $L_{2-10\,\mathrm{keV}}$, but we can also determine whether this approach to correcting for the host galaxy reproduces the $L_{12\,\mu\mathrm{m}}-L_{2-10\,\mathrm{keV}}$ relation. We select from the host galaxy SED templates for different luminosity bins presented in Silva et al. (2004) using our estimate of $L_{2-10\,\mathrm{keV}}$ from the BAT data. In a few cases where 60 or 100 μm data were not available, the normalization of the host template was tied to the nuclear template normalization, to provide a sensible estimate of host galaxy contamination based on the observations of Silva et al. (2004) in their sample of AGN. Some example SEDs with both host and nuclear SED templates fitted are shown in Fig. 8. We also present the distribution of $L_{12\,\mu\mathrm{m}}$ against $L_{2-10\,\mathrm{keV}}$ in Fig. 5, with the nuclear $L_{12\,\mu\mathrm{m}}$ determined from the 12 μm flux of the nuclear part of the SED fit only.

In the absence of high-resolution data for a large fraction of our sample, these methods for removing the host galaxy can only go so far in tackling this complex issue. In Fig. 6, we present a comparison of our uncorrected *IRAS* fluxes with the accurate nuclear VLT/VISIR fluxes from Gandhi et al. (2009). It can be seen that in some cases the degree of host contamination in the *IRAS* fluxes can be very large (e.g. NGC 4388); while in others the *IRAS* fluxes are almost identical to the nuclear fluxes from VISIR/VLT (e.g. NGC 6300), indicating that no correction for contamination is necessary. The two methods presented here go some way in accounting for aperture effects, but as discussed by Horst et al. (2008) higher resolution IR data which isolate the nuclear emission are ultimately much preferred.

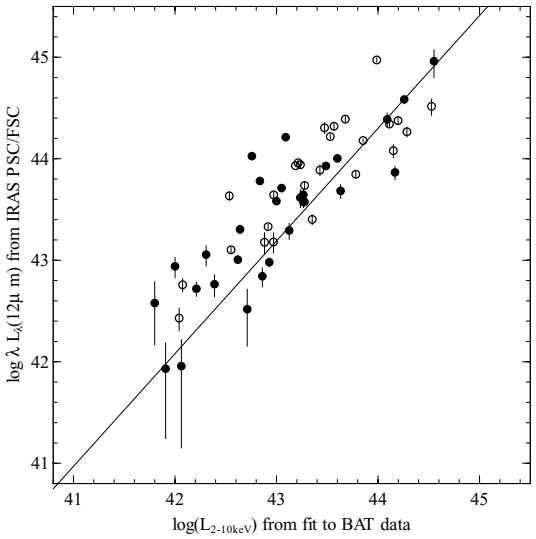

Figure 5. Nuclear 12 μm luminosity against 2–10 keV luminosity from fits to BAT data, from combined host and nuclear IR SED template fitting to the IRAS 12–100 μm data.

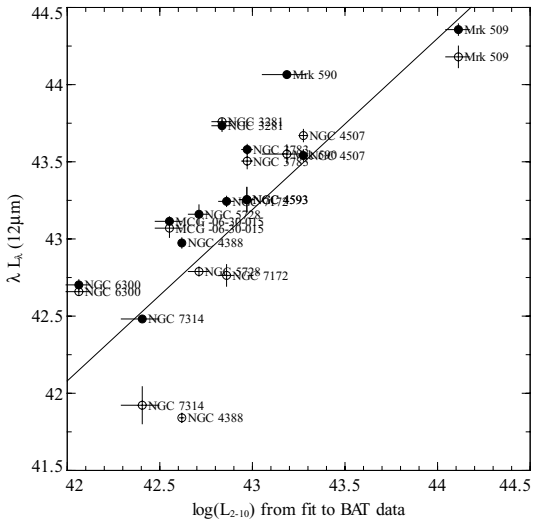

Figure 6. IR 12 μm luminosity against 2–10 keV luminosity from fits to BAT data. Black points are *IRAS* data uncorrected for host galaxy contamination, and empty circles show the nuclear 12 μm luminosity from the VISIR/VLT data presented in Gandhi et al. (2009).

3.2.3 Total nuclear IR luminosity

We broadly follow the approach of Pozzi et al. (2007) outlined in their study on high-redshift, luminous, obscured quasars and fit the nuclear and host galaxy templates from Silva et al. (2004) to our data. The appropriate nuclear template from Silva et al. (2004) is selected based on the absorbing column $N_{\rm H}$ reported in Winter et al. (2009). The fitting is performed using a simple least-squares algorithm from the SCIPY suite of functions available for use with the PYTHON programming language. If the host galaxy contamination is removed via method 1 (Section 3.2.1) above, we only fit the 12–25 μm data and correct the integrated nuclear IR luminosity by the fraction given by equation (1). If method 2 (Section 3.2.2) is used, only the nuclear component of the fit is integrated. The observed IR luminosity is then obtained by integration of the nuclear template between 1 and 1000 μm.

We reiterate briefly here that the absorptions seen in X-rays and the amount of dust responsible for reddening the optical–UV SED/producing the reprocessed IR do not necessarily match (e.g. Maiolino & Risaliti 2007). This calls into question the use of the X-ray $N_{\rm H}$ for selecting the template to use from Silva et al. (2004); however, the fact that Silva et al. (2004) find from observations that the IR SED shapes of AGN can be broadly grouped on $N_{\rm H}$ would argue for at least a statistical correlation between the two types of absorption, in addition to the findings from surveys discussed in Section 1. In this first-order approach, the selection of nuclear SED template based on $N_{\rm H}$ is therefore sensible.

Under method (2) for host galaxy removal, a few objects (Mrk 841, NGC 612, PGC 13946, 2MASX J04440903+2813003, EXO 055620−3820.2, 4U 1344−60, ESO 297−018, NGC 7314) yield a fit with zero nuclear component and only a host galaxy component. These probably represent cases where the host galaxy contamination is very large and the nucleus is too buried to get an accurate estimate of its presence from our simple SED fitting alone. We exclude these objects from the results from method (2) due to these uncertainties. A detailed exploration of the different host and nuclear SED models may be able to yield more satisfactory fits in these cases, but is beyond the scope of this paper.

To convert this observed IR luminosity into a measure of the reprocessed nuclear accretion disc luminosity, correction factors are required to account for the geometry of the torus and the anisotropy of the torus emission. We adopt the same approach as Pozzi et al. (2007) in correcting for these effects. The correction for geometry relates to the covering factor f which obscures the optical–UV emission from the accretion disc from view. Their geometry correction is based on a statistical argument, employing the ratio of obscured to unobscured quasars as found by recent X-ray background synthesis models (Gilli, Comastri & Hasinger 2007) to infer a typical torus covering fraction of $f \approx 0.67$. This value is also consistent with the covering fraction obtained from recent detailed clumpy torus models (Nenkova et al. 2008b), for typical torus parameters (e.g. number of line-of-sight clouds ∼5, with an opening angle of ∼30°–45°). Inverting this, we obtain a factor of ∼1.5 by which the observed IR nuclear luminosity needs to be multiplied to obtain the total optical–UV accretion emission. Pozzi et al. (2007) estimate the anisotropy correction factors by computing the ratio of the luminosities from face-on versus edge-on AGN (with the column density $N_{\rm H}$ parameterizing the inclination of the torus). They normalize the Silva et al. (2004) templates for all different $N_{\rm H}$ values to have the same 30–100 μm luminosities. The luminosity ratios for face-on to edge-on AGN are then calculated in the 1–30 μm range, where the effects of anisotropy are most pronounced. They obtain values of ∼1.2–1.3 for $10^{22} < N_{\rm H} < 10^{24}$ cm^{-2} and ∼3–4 for $N_{\rm H} > 10^{24}$ cm^{-2} sources. For face-on (low-absorption $\log N_{\rm H} < 22$) sources, no correction is necessary. We adopt a simple approach, using values of 1.3 for $22 < \log N_{\rm H} < 24$ sources and 3.5 for $\log N_{\rm H} > 24$ sources.

4 CALCULATING THE TOTAL POWER OUTPUT

We present some of the SEDs constructed from the *IRAS* and BAT data in Figs 7 and 8. The bolometric luminosity $L_{\rm bol}$ is calculated as the sum of the nuclear IR luminosity $L_{\rm IR,corr}$ (corrected for torus geometry, anisotropy of emission and non-nuclear contamination as detailed above) and the total X-ray luminosity, $L_{0.5-100\,{\rm keV}}$. For the high-absorption objects, we multiply the power-law by an intrinsic absorption component (the WABS model in XSPEC, using the value of $N_{\rm H}$ from Winter et al. 2009) before calculating $L_{0.5-100\,{\rm keV}}$ to

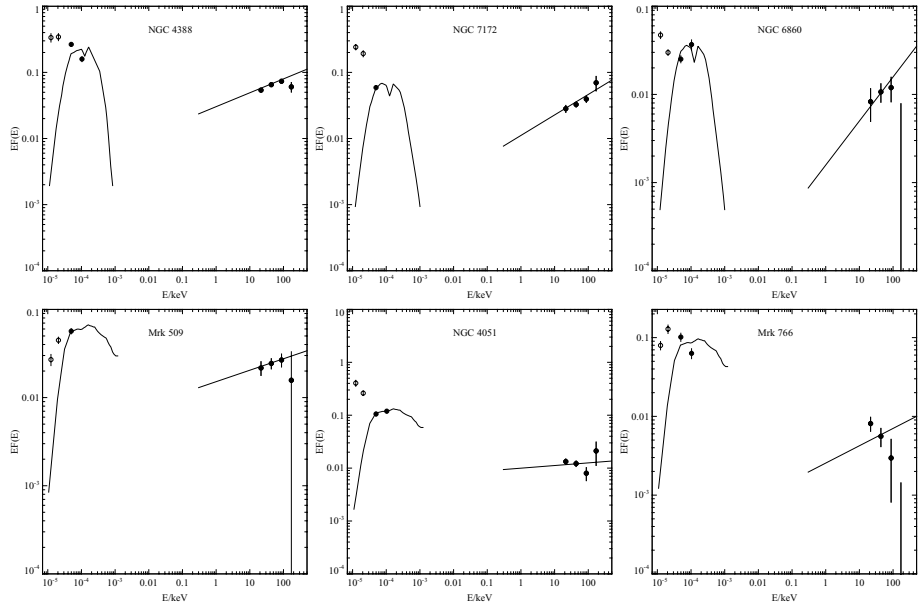

Figure 7. Some example SEDs with *IRAS* and BAT data. Data points used in the fit (IRAS and BAT) are shown with filled black circles. Model fits are represented by the solid black lines. Only 12–25 μm *IRAS* data are used to fit the IR nuclear templates; longer wavelength (lower energy) 60 and 100 μm data are shown for information (unfilled circles). The nuclear luminosities from the fit are corrected for host contribution using method 1 (Section 3.2.1).

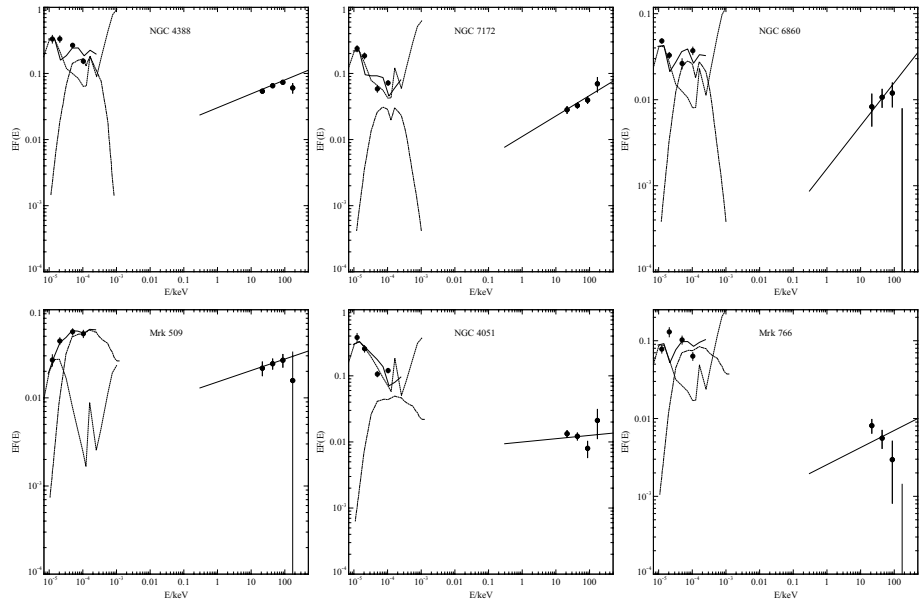

Figure 8. Some example SEDs with *IRAS* and BAT data, with both host and nuclear SED fitting (Section 3.2.2). Data points (*IRAS* and BAT) are shown with filled black circles. The full model fit is represented by solid black lines; the dotted and dot–dashed lines show the host and nuclear components, respectively.

avoid double-counting part of the X-ray luminosity which is reprocessed to the IR, in line with the approach of Pozzi et al. (2007). For low-absorption objects, the difference between the intrinsic and absorption-corrected 0.5–100 keV luminosities are found to be negligible, so we leave out this step for that class. We also extract the absorption-corrected $L_{2-10\,\mathrm{keV}}$ for calculating bolometric corrections $\kappa_{2-10\,\mathrm{keV}} = L_{\mathrm{bol}}/L_{2-10\,\mathrm{keV}}$.

We also calculate Eddington ratios for our sample using black hole mass (M_{BH}) estimates. For all but one object (Cyg A), these are calculated from the $M_{\mathrm{BH}}-L_{\mathrm{K,bulge}}$ relation (where L_{bulge} is the host galaxy K-band bulge luminosity), for consistency with the work of Vasudevan et al. (2009). We use the Marconi & Hunt (2003) formulation for this relation, using an identical method to determine the bulge luminosity as that outlined in Vasudevan et al. (2009). For Cyg A, the dynamical mass estimate from Tadhunter et al. (2003) is used as discussed in Section 2. Eddington ratios are calculated using $\lambda_{\mathrm{Edd}} = L_{\mathrm{bol}}/L_{\mathrm{Edd}}$ for Eddington luminosities $L_{\mathrm{Edd}} = 1.3 \times 10^{38}(M_{\mathrm{BH}}/\mathrm{M}_{\odot})\,\mathrm{erg\ s^{-1}}$.

4.1 Calibrating the method

We first attempt to estimate the accuracy of our bolometric luminosity calculation using IR and hard X-ray emission. Brocksopp et al. (2006) and Vasudevan & Fabian (2009) (and references therein)

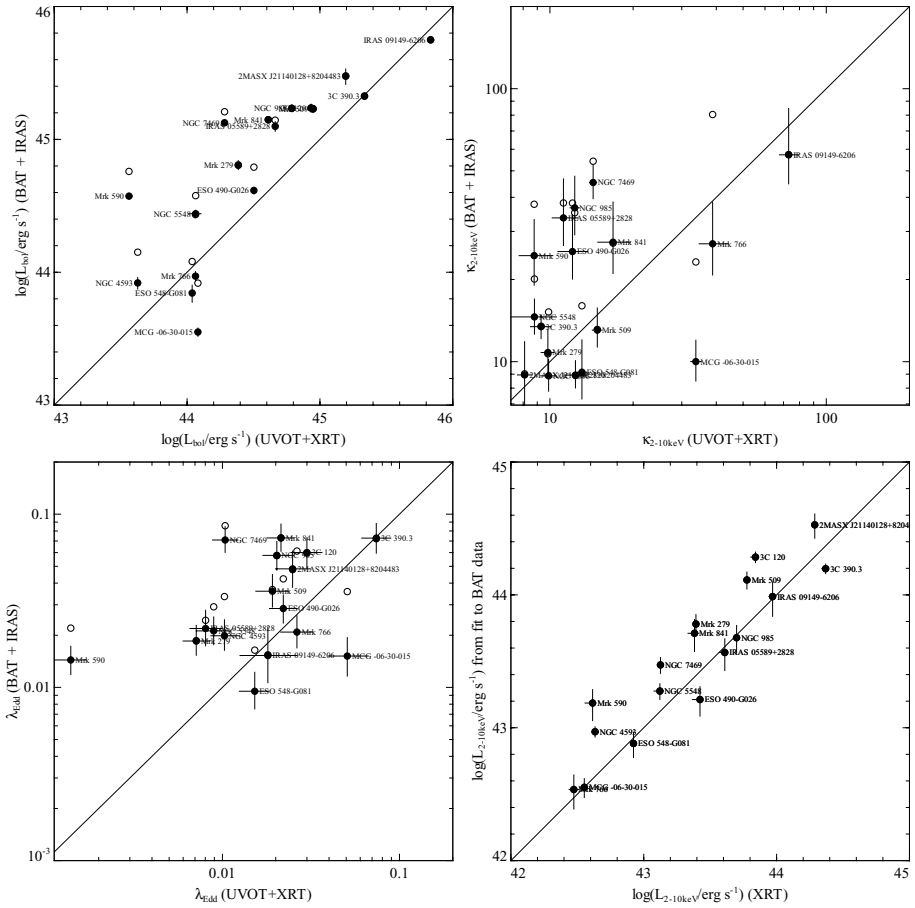

Figure 9. Comparison between values of bolometric luminosity, 2–10 keV bolometric corrections, Eddington ratios and 2–10 keV luminosities using the time-averaged, non-contemporaneous *IRAS* and BAT data and the method from Vasudevan et al. (2009) using simultaneous optical, UV and X-ray data from *Swift*. The solid lines represent the desired 1 : 1 correlation, and empty circles show the results before correcting for host galaxy contamination of *IRAS* fluxes. Host galaxy correction to *IRAS*-determined IR luminosities as detailed in Section 3.2.1.

outline the approach of using simultaneous optical, UV and X-ray data for calculation of intrinsic SEDs, and this approach is developed further using *Swift* XRT and UVOT data in Vasudevan et al. (2009) for low-absorption objects in the *Swift*/BAT 9-month catalogue. Using IR along with long-exposure BAT data produces a long-term averaged estimate of $L_{\rm bol}$ in contrast to the 'snapshot' approach from using simultaneous optical-to-X-ray data, but statistically one expects reasonable agreement between the two approaches, since the effects of variability should be averaged out when considering a large enough sample. We present comparisons between the values of $L_{\rm bol}$, $\kappa_{2-10\,{\rm keV}}$, $\lambda_{\rm Edd}$ and $L_{2-10\,{\rm keV}}$ from Vasudevan et al. (2009) and this study in Figs 9 and 10, for the two different host-contamination removal methods. There are 17 objects overlapping between the two studies.

The bolometric luminosities determined from both methods agree reasonably well with those determined from UVOT and XRT fits, but both methods show a systematically larger $L_{\rm bol}$ than that determined from UVOT and XRT data. In particular, the degree of host galaxy contamination removed from fitting nuclear and host SEDs (method 2) yields estimates for $L_{\rm bol}$ about 0.3–0.4 dex larger than the optical-to-X-ray estimates. This could be attributed to a number of factors: firstly it is possible that the simple SED fitting (in method 2) underestimates the host galaxy contribution and more correction is necessary; secondly, the geometry and anisotropy corrections assumed in scaling the observed IR luminosity could be too large for many of the objects where poor agreement is reported, and thirdly the estimates from UVOT–XRT could themselves be too small (the latter two phenomena would apply equally to methods 1 and 2). The $L_{\rm bol}$ from the UVOT and XRT fit depends on the black hole mass and tends to increase as the black hole mass decreases; Vasudevan et al. (2009) discuss the possibility that the mass could be overestimated by about a factor of $\sim$2 which could alleviate the discrepancy seen here. The problem is a complex one and ultimately requires better knowledge of the torus-covering fraction (which may have a very broad distribution; e.g. Rowan-Robinson, Valtchanov & Nandra 2009) and emission characteristics to perform this comparison more accurately.

The distributions of bolometric correction and Eddington ratio are more clustered, so a correlation between the two approaches is difficult to discern. The finding of a low distribution of Eddington ratios in Vasudevan et al. (2009) is, however, broadly confirmed with the *IRAS* and BAT method. The notable outlier Mrk 590 is known from the literature to have a very reddened optical–UV spectrum (confirmed with UVOT), and constraining the Big Blue Bump shape using the *K*-band mass estimate yields a poor fit in Vasudevan et al. (2009). If for this particular source we employ the results obtained from using the reverberation mass instead, its accretion rate lies much closer to the line of one-to-one correspondence, moving to join the cluster of points around $\lambda_{\rm Edd} \sim 0.02$. Despite the scatter however, the general trend for agreement between the two

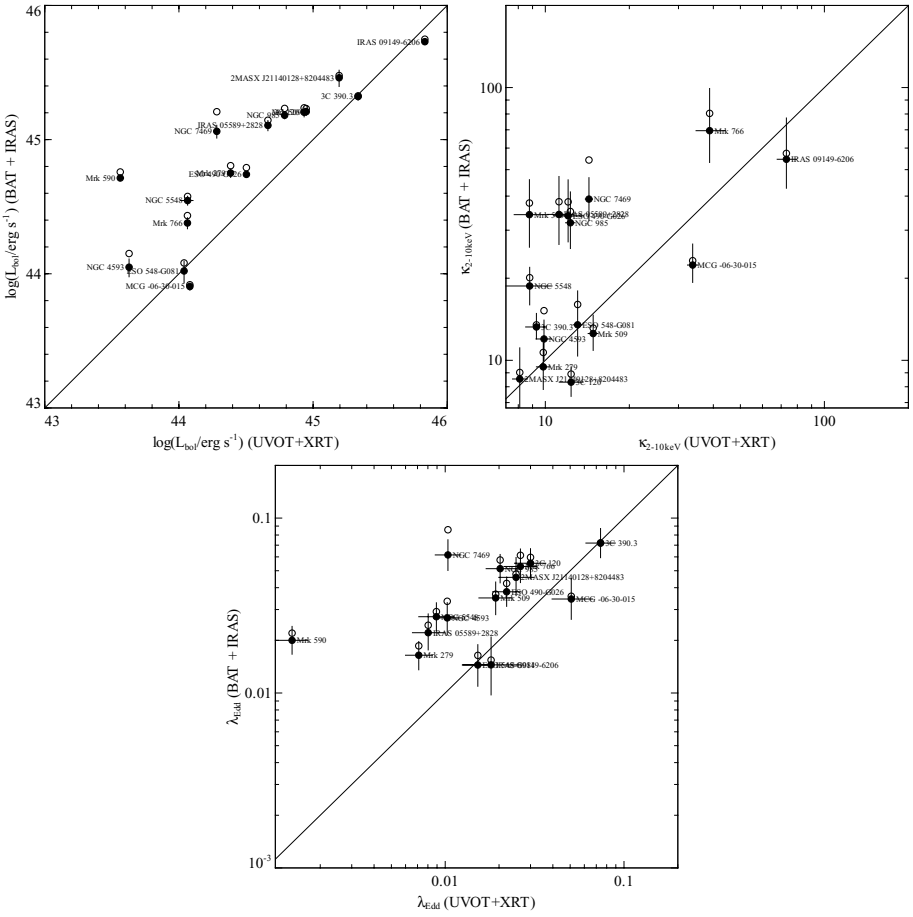

Figure 10. Comparison between values for bolometric luminosity, 2–10 keV bolometric corrections, Eddington ratios and 2–10 keV luminosities from *IRAS* and BAT data with the results from *Swift* UVOT–XRT data presented in Vasudevan et al. (2009). Host galaxy in IR accounted for as detailed in Section 3.2.2. Key as in Fig. 9.

methods motivates us to continue in our attempts at addressing the key questions of this study.

We also present some of the SEDs for the objects with XRT and UVOT data, now including the *IRAS* and BAT data (Fig. 11). There is some variation between the photon index used for fitting the BAT data and that found from the XRT data in Vasudevan et al. (2009), but generally both data sets show similar values.

5 RESULTS AND DISCUSSION: BOLOMETRIC CORRECTIONS AND EDDINGTON RATIOS

We present the bolometric corrections and Eddington ratios obtained in Figs 12 and 13. The distributions are plotted as histograms in Fig. 14 and numerical values are provided in Table 2. The values obtained from fitting a nuclear SED template to the IR data without any host galaxy correction are shown using empty circles for comparison, and objects from the 3C catalogues (3C 382, 3C 120, 3C 390.3 and 3C 403) are highlighted with blue squares, for easy identification in case some degree of jet contribution to the flux affects the results for these objects.

For low-absorption objects, the statistical correction method for removing the host galaxy results in bolometric corrections of ∼19 on average with Eddington ratios centred around ∼0.035 (Fig. 12, left-hand panel). In contrast, using the SED fitting approach yields $\langle\kappa_{2-10\,\mathrm{keV}}\rangle \sim 24$ with $\langle\lambda_{\mathrm{Edd}}\rangle \sim 0.039$ (Fig. 13, left-hand panel). Both are generally consistent with the finding of low bolometric corrections for unabsorbed objects from Vasudevan et al. (2009), but the host SED fitting approach does have a greater proportion of objects at higher bolometric corrections.

The object consistently exhibiting the largest bolometric correction in the high absorption subsample is NGC 1365, which is one of two possible borderline Compton-thick objects in that sample and known to have variable absorption as discussed in Section 3.1. If the source was predominantly in a Compton-thick state during the BAT period of observation, the BAT flux would be substantially lower than the intrinsic AGN flux as pointed out in Section 3.1, giving an artificially high bolometric correction. Additionally, this object is known to exhibit a nuclear starburst (Strateva & Komossa 2009 and references therein) so is particularly susceptible to a high level of starburst contamination in the IR fluxes, which may not have been completely removed by either method of host galaxy removal. Both of these effects would serve to increase the bolometric correction to an abnormally high value. A more detailed object-specific analysis is needed to check whether the bolometric correction for this object is intrinsically high.

For high-absorption objects, the statistical approach to correcting for the host galaxy (Fig. 12, right-hand panel) yields a wider spread of bolometric corrections than for low-absorption objects, but values are still centred on low values ($\langle\kappa_{2-10\,\mathrm{keV}}\rangle \sim 15$) with a predominantly low Eddington ratio distribution ($\langle\lambda_{\mathrm{Edd}}\rangle \sim 0.034$). However, under the host SED correction method, some notable outliers with negligible host galaxy component are located near

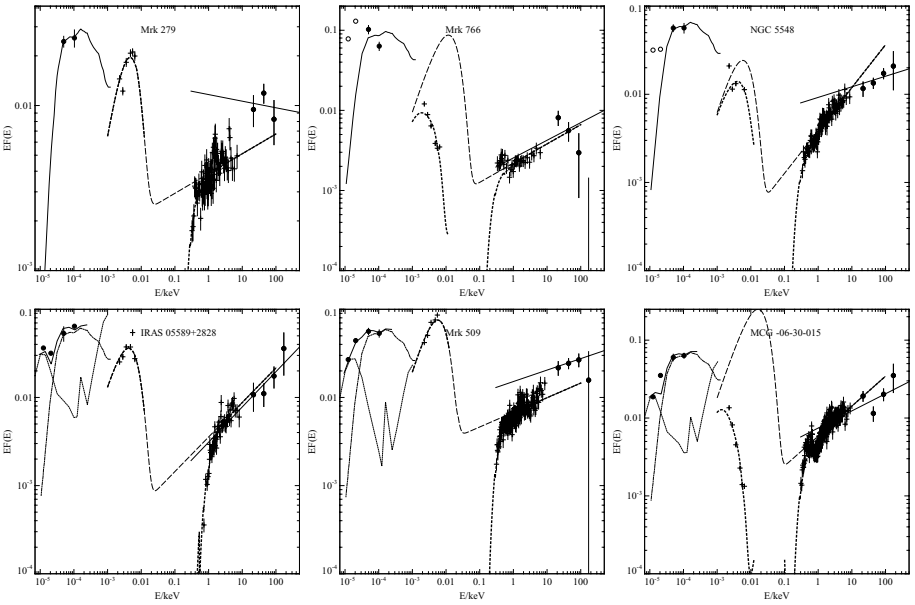

Figure 11. A selection of SEDs with *IRAS*, UVOT, XRT and BAT data. Key as in Fig. 7 with the following additions: crosses represent simultaneous UVOT and XRT data, heavy dotted lines represent the fits to those data with intrinsic absorption included (optical–UV reddening and X-ray absorption) and dashed lines represent the dereddened, absorption-corrected SED fit from which bolometric luminosities were estimated in Vasudevan et al. (2009). The top three SEDs show the fitting of only a nuclear IR SED with host galaxy contamination corrected for afterwards as detailed in Section 3.2.1; the lower three show the combined fitting of nuclear and host galaxy SED templates in the IR as described in Section 3.2.2.

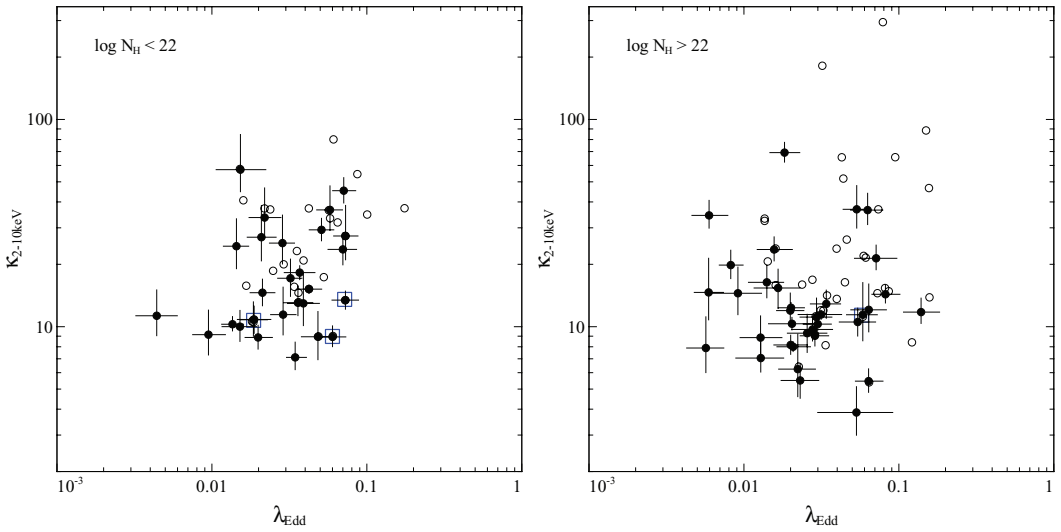

Figure 12. Bolometric corrections against Eddington ratios for low-absorption (left-hand panel) and high-absorption (right-hand panel) objects, with statistical correction for non-nuclear contamination of *IRAS* fluxes (black filled points) as detailed in Section 3.2.1. Results before applying the contamination correction are shown for comparison (empty circles). Objects highlighted with blue squares are from the 3C catalogue; these radio-loud objects are demarcated to identify objects in which some jet contribution might be affecting the results.

$\lambda_{Edd} \sim 0.1$ with bolometric corrections of $\sim$80. These outliers are (from highest bolometric correction downwards) NGC 1365, IC 5063, MCG −03-34-064 and NGC 3281. In the case of NGC 3281, the degree of host contamination is known to be small from the comparison with VLT/VISIR fluxes in Fig. 6, so the high accretion rate and value of $\kappa_{2-10\,keV}$ may be real for such objects (bearing in mind the caveats regarding NGC 1365 discussed above). Inspection of the host and nucleus SED fits for these four objects in Fig. 15 implies sensible estimation of the host contamination, implying that method 1 has overestimated the nuclear contamination for these sources. The large bolometric corrections from method 2 for these objects may therefore, on average, be closer to the true values. These objects could then potentially be part of the 'transition region' to high bolometric corrections at and above $\lambda_{Edd} \sim 0.1$ postulated by Vasudevan & Fabian (2007), (2009). Under method 2 for host galaxy correction, at $\lambda_{Edd} < 0.03$, bolometric corrections have an average value of $\sim$15, increasing to a value of $\sim$32 for $0.03 < \lambda_{Edd} < 0.2$ (the average Eddington ratio for the whole sample is $\sim$0.043). This could be a preliminary indication of a significant minority of higher accretion rate objects amongst high-absorption AGN and may provide tentative evidence that the Eddington ratio-dependent bolometric correction scheme of Vasudevan & Fabian (2007) may

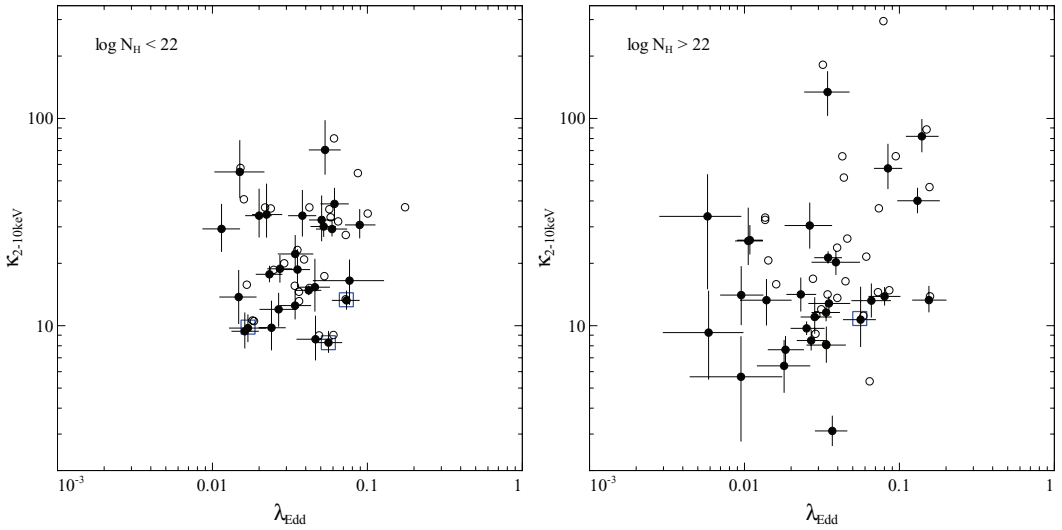

Figure 13. Bolometric corrections against Eddington ratios for low-absorption (left-hand panel) and high-absorption (right-hand panel) objects, where the host galaxy/starburst contribution in the IR has been removed by SED fitting as detailed in Section 3.2.2; key as in Fig. 12.

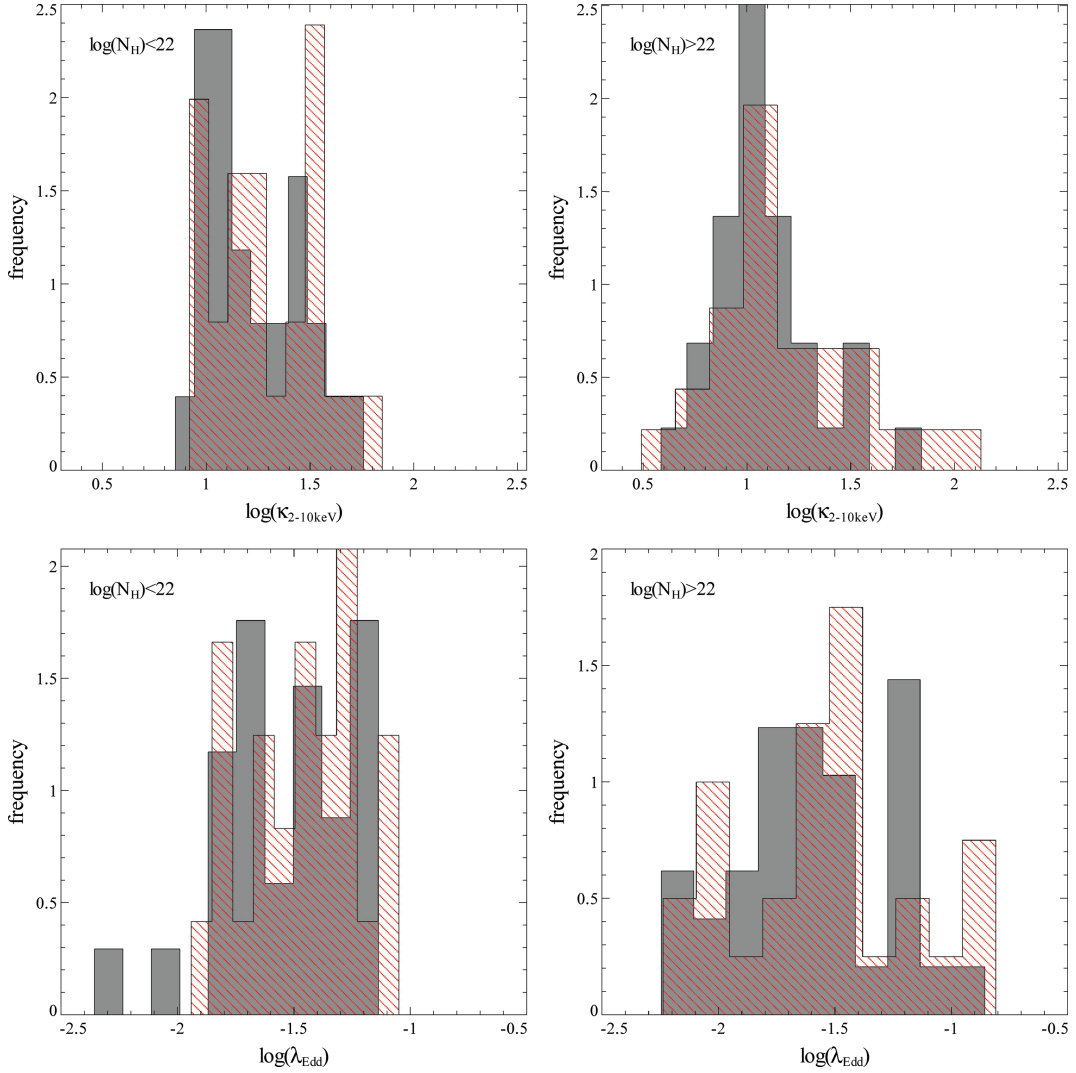

Figure 14. Histograms of bolometric correction and Eddington ratio distributions. The grey filled histograms are obtained from the statistical method of host galaxy correction in the IR, whereas the hatch-filled histograms are from host galaxy SED fitting to remove IR galaxy contamination.

Table 2. Table of results from analysis of IRAS–BAT SEDs.

AGN	L_X[a]	$L_{1-1000\,\mu m}$[b]	L_{bol}[c]	$\kappa_{2-10\,keV}$[d]	$\kappa_{12\,\mu m}$[e]	M_{BH}[f]	λ_{Edd}[g]
			– (low N_H) –				
2MASX J21140128+8204483	45.1, 44.5	45.3/45.2	45.5/45.5	8.94/8.60	9.62/8.79	8.68	0.048/0.046
3C 120	44.8, 44.3	45.0/45.0	45.2/45.2	8.93/8.29	8.51/8.67	8.35	0.060/0.056
3C 382	44.9, 44.2	44.9/44.8	45.2/45.1	10.8/9.74	8.10/11.5	8.79	0.019/0.017
3C 390.3	44.9, 44.2	45.1/45.1	45.3/45.3	13.4/13.2	9.06/8.90	8.35	0.073/0.073
ESO 490-G026	43.8, 43.2	44.5/44.7	44.6/44.7	25.3/34.0	7.51/6.01	8.05	0.029/0.038
ESO 511-G030	43.9, 43.4	44.2/44.1	44.4/44.3	11.4/9.77	–/8.59	7.84	0.029/0.024
ESO 548-G081	43.4, 42.9	43.6/43.9	43.8/44.0	9.15/13.8	5.40/7.10	7.74	0.0095/0.015
IC 4329A	44.4, 43.9	44.9/44.9	45.0/45.0	15.2/14.8	7.05/7.01	8.29	0.042/0.042
IRAS 05589+2828	44.2, 43.6	45.0/45.0	45.1/45.1	33.6/34.4	5.56/6.11	8.64	0.022/0.022
IRAS 09149-6206	44.6, 44.0	45.7/45.7	45.7/45.7	57.2/55.2	6.16/5.71	9.45	0.015/0.015
MCG −06-30-015	43.1, 42.6	43.3/43.8	43.6/43.9	10.0/22.2	8.58/6.32	7.25	0.015/0.034
MCG +08-11-011	44.2, 43.5	44.9/44.9	45.0/45.0	29.3/30.1	7.85/6.18	8.17	0.051/0.052
Mrk 279	44.3, 43.8	44.6/44.6	44.8/44.8	10.8/9.40	7.69/8.05	8.42	0.019/0.016
Mrk 290	43.9, 43.3	44.2/44.3	44.4/44.4	13.0/15.3	7.95/7.48	7.67	0.039/0.046
Mrk 509	44.7, 44.1	45.1/45.1	45.2/45.2	13.1/12.5	7.46/7.40	8.56	0.036/0.034
Mrk 590	43.8, 43.2	44.5/44.7	44.6/44.7	24.5/34.0	5.30/6.04	8.30	0.014/0.020
Mrk 766	43.1, 42.5	43.9/44.4	44.0/44.4	27.0/70.5	8.09/5.56	7.53	0.021/0.053
Mrk 79	44.0, 43.4	44.6/44.6	44.7/44.7	17.1/18.7	8.04/6.42	8.04	0.032/0.035
Mrk 841	44.3, 43.7	45.1/–	45.1/–	27.4/–	4.81/–	8.17	0.073/–
NGC 3516	43.5, 42.9	43.7/44.0	43.9/44.2	10.3/17.7	8.72/6.80	7.68	0.014/0.023
NGC 3783	43.6, 43.0	44.1/44.4	44.2/44.4	18.2/29.3	9.08/6.22	7.55	0.037/0.059
NGC 4051	42.6, 42.0	42.6/43.2	42.9/43.3	7.11/16.5	9.74/6.61	6.26	0.035/0.077
NGC 4593	43.5, 43.0	43.7/43.9	43.9/44.1	8.87/12.0	10.4/7.46	7.51	0.020/0.027
NGC 5548	43.8, 43.3	44.3/44.5	44.4/44.5	14.6/18.8	7.23/6.43	8.00	0.021/0.027
NGC 7213	42.7, 42.1	42.9/43.5	43.1/43.5	11.3/29.3	6.47/6.02	7.37	0.0044/0.011
NGC 7469	44.0, 43.5	45.1/45.0	45.1/45.1	45.3/38.7	8.62/5.70	8.16	0.071/0.061
NGC 931	43.8, 43.2	44.5/44.7	44.6/44.7	23.6/30.6	6.31/6.01	7.65	0.070/0.089
NGC 985	44.3, 43.7	45.2/45.1	45.2/45.2	36.6/32.4	6.08/6.17	8.36	0.058/0.051
			– (high N_H) –				
2MASX J04440903+2813003	43.3, 42.7	43.3/–	43.6/–	8.86/–	–/–	7.37	0.013/–
3C 403	44.5, 44.1	45.0/45.0	45.1/45.1	11.4/10.7	5.96/5.49	8.26	0.059/0.056
4U 1344-60	43.5, 43.0	43.9/–	44.1/–	12.9/–	7.56/–	7.44	0.034/–
Cyg A	45.0, 44.6	45.7/45.6	45.7/45.7	15.4/13.3	–/5.19	9.41†	0.017/0.014
ESO 005-G004	42.6, 41.9	42.9/42.6	43.1/42.9	14.5/9.26	5.89/9.19	6.98	0.0091/0.0059
ESO 103-035	43.7, 43.5	44.5/44.6	44.6/44.6	11.8/13.3	7.73/4.81	7.30	0.14/0.16
ESO 297-018	43.9, 43.2	44.0/–	44.2/–	9.31/–	–/–	7.69	0.026/–
ESO 506-G027	44.2, 43.6	44.4/44.3	44.6/44.6	9.04/8.48	7.64/7.53	8.02	0.029/0.027
EXO 055620-3820.2	44.3, 43.8	45.2/–	45.2/–	23.6/–	4.74/–	8.90	0.016/–
IC 5063	43.3, 42.8	44.3/44.7	44.3/44.7	36.5/82.0	6.59/4.45	7.41	0.063/0.14
MCG −03-34-064	43.4, 43.1	44.6/44.8	44.7/44.9	36.8/57.4	6.23/4.37	7.81	0.053/0.084
Mrk 1498	44.6, 44.3	45.2/45.2	45.3/45.3	11.1/11.0	4.65/5.23	8.72	0.029/0.028
Mrk 18	42.9, 42.4	43.0/43.4	43.3/43.5	7.89/14.1	7.63/5.85	7.42	0.0057/0.0095
Mrk 3	43.9, 43.6	44.7/44.7	44.8/44.7	14.3/13.8	8.50/5.47	7.72	0.082/0.080
Mrk 348	43.7, 43.2	44.1/44.2	44.3/44.4	10.5/13.2	7.26/5.49	7.41	0.054/0.066
Mrk 6	43.7, 43.0	44.2/44.4	44.3/44.5	19.8/25.9	6.79/5.67	8.31	0.0082/0.011
NGC 1142	44.1, 44.2	44.8/44.5	44.9/44.7	5.46/3.11	6.56/6.24	7.98	0.064/0.037
NGC 1365	42.4, 42.0	43.8/44.1	43.8/44.1	69.2/134	10.0/15.1	7.46*	0.018/0.034
NGC 2110	43.6, 42.9	43.5/43.7	43.8/43.9	8.00/9.71	11.9/8.69	7.40	0.021/0.025
NGC 2992	43.0, 42.3	43.4/43.7	43.5/43.8	16.4/30.4	7.33/5.54	7.27	0.014/0.026
NGC 3227	42.9, 42.2	43.0/43.4	43.2/43.5	10.3/20.2	10.4/6.27	6.80*	0.020/0.039
NGC 3281	43.3, 42.8	44.1/44.4	44.2/44.4	21.4/40.1	6.38/4.57	7.20	0.071/0.13
NGC 4388	43.0, 42.6	43.6/43.6	43.7/43.7	11.4/12.8	7.83/5.26	7.07	0.032/0.035
NGC 4507	43.8, 43.3	44.1/44.2	44.3/44.3	10.3/11.6	8.17/5.83	7.70	0.030/0.034
NGC 526A	43.7, 43.3	44.2/44.3	44.3/44.4	12.0/14.2	6.79/5.87	7.93	0.020/0.023
NGC 5506	43.5, 43.0	44.0/44.3	44.1/44.3	12.3/21.3	7.80/5.53	7.67	0.020/0.035
NGC 5728	43.3, 42.7	43.5/43.1	43.7/43.5	9.70/6.40	10.3/10.2	7.15*	0.028/0.018
NGC 612	43.7, 43.7	44.4/–	44.5/–	6.24/–	3.01/–	8.01	0.022/–
NGC 6300	42.4, 42.1	42.7/42.6	42.9/42.8	7.06/5.67	8.26/7.17	6.70*	0.013/0.0095
NGC 6860	43.3, 42.6	43.6/44.0	43.8/44.1	14.6/25.6	6.25/5.63	7.91	0.0059/0.011
NGC 7172	43.4, 42.9	43.6/43.5	43.8/43.7	8.16/7.66	7.53/7.94	7.36	0.020/0.018

Table 2 – *continued*

AGN	L_X[a]	$L_{1-1000\,\mu m}$[b]	L_{bol}[c]	$\kappa_{2-10\,keV}$[d]	$\kappa_{12\,\mu m}$[e]	M_{BH}[f]	λ_{Edd}[g]
NGC 7314	42.7, 42.4	42.7/–	43.0/–	3.86/–	11.3/–	6.14	0.053/–
NGC 7582	42.5, 41.8	43.3/43.3	43.3/43.3	34.4/33.7	9.23/5.53	7.44*	0.0060/0.0058
NGC 788	43.4, 43.1	43.7/43.9	43.9/44.0	5.50/8.06	6.67/5.56	7.39	0.023/0.034
PGC 13946	43.9, 43.3	44.2/–	44.4/–	12.1/–	–/–	7.46	0.064/–

Note. Luminosities L are presented as $\log(L)$ with L given in erg s^{-1} .[a]Total (0.5–100 keV, first value), followed by 2–10 keV (second value) X-ray luminosity, using the photon index Γ from Winter et al. (2009) (requiring $1.5 < \Gamma < 2.2$). Errors (in luminosity) are typically ∼10– 20 per cent. [b]Total integrated nuclear IR luminosity, with geometry, anisotropy and non-nuclear contamination correction factors applied (see the text). The first value includes the statistical host galaxy correction based on $L_{2-10\,keV}$, and the second value is that obtained from combined nuclear and host SED template fitting. Errors are typically ∼5–10 per cent. [c]Bolometric luminosity ($L_{0.5-100\,keV} + L_{1-1000\,\mu m}$). Values from both methods of host galaxy removal provided, as for *c*. Errors are typically ∼5 per cent. [d]2–10 keV bolometric correction $\kappa_{2-10\,keV} = L_{bol}/L_{2-10\,keV}$, with statistical host galaxy removal/host+nucleus SED fitting methods. [e]Bolometric correction for observed nuclear 12 μm monochromatic luminosity $\kappa_{12\,\mu m} = L_{bol}/(\lambda\ L_{\lambda}^{12\,\mu m})$, for two different methods of host galaxy removal. [f]Logarithm of black hole mass from *K*-band bulge magnitude estimate (in solar masses). Errors are typically ∼0.1 dex, but for a discussion of systematics see Vasudevan et al. (2009). *Masses marked with an asterisk are likely to have the bulge luminosity, and hence black hole mass, underestimated: see the text for details. †We use the dynamical mass from Tadhunter et al. (2003) for Cyg A; since its bulge is abnormally large by virtue of being a cD galaxy, the use of the 2MASS PSC is not valid and would underestimate the mass by a factor of ∼30. [g]Eddington ratio $\lambda_{Edd} = L_{bol}/L_{Edd}$, using both methods of host galaxy removal. Random errors are typically ∼10–20 per cent.

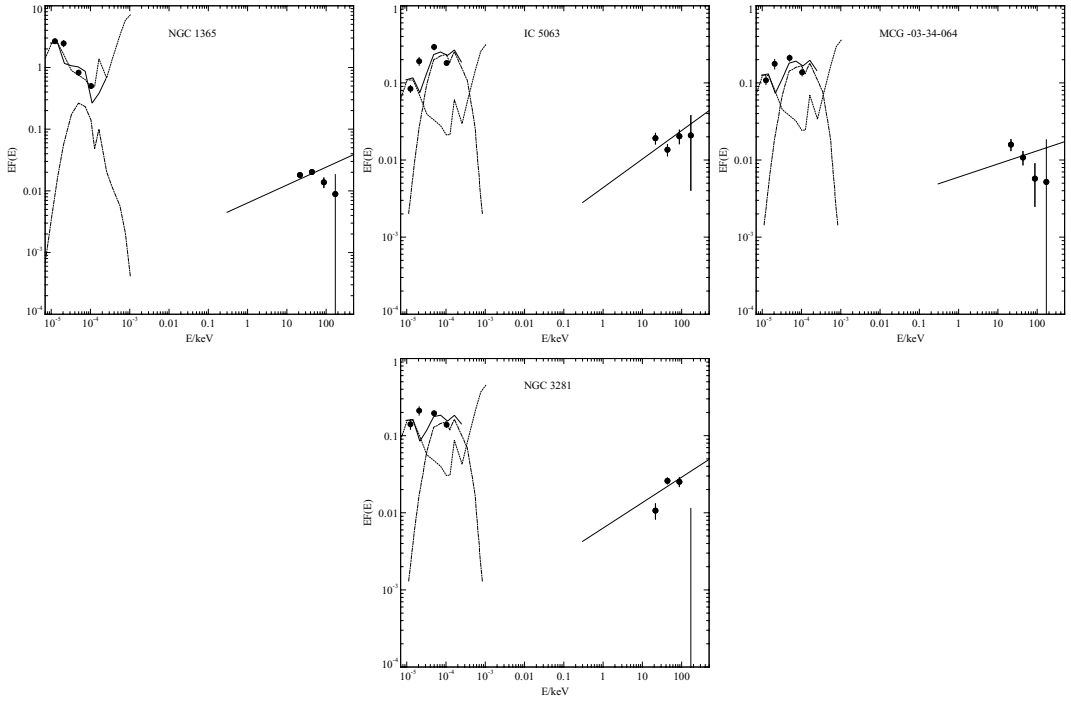

Figure 15. SEDs for the four objects with high bolometric corrections and Eddington ratios, under method 2 (Section 3.2.2) for host galaxy removal. Key as in Fig. 8.

be borne out in high-absorption AGN. Better constraints on the nuclear MIR emission and black hole mass are needed to confirm this, however.

Under the statistical method for host-galaxy correction (method 1), fitting both 25 and 12 μm points for objects with particularly 'red' 12–25 μm SEDs to a nuclear SED template results in a fit inconsistent with the 12 μm datum. Such SED shapes probably imply that the nuclear 25 μm luminosity is primarily from the host galaxy rather than the nucleus, and fitting to only the 12 μm point would be more robust. We estimated the effect of this on the results by fitting only the 12 μm for the handful objects with such SEDs, and find that the resultant bolometric luminosities are altered on average by a few per cent (the largest change is for NGC 7582, causing a reduction of 40 per cent in the total IR luminosity). Overall, such modifications do not produce any significant changes in the results. More detailed model fits to better quality IR data in the future could be fit using a more considered approach.

We note that a few AGN excluded from the 'host-plus-nucleus' SED fit subsample due to the fit yielding zero nuclear contribution (see Section 3.2.3) are more likely to have very small nuclear IR luminosities, therefore would be expected to lie at lower bolometric corrections and Eddington ratios; this would not be expected to alter the distributions seen significantly.

These results are illuminating for our understanding of accretion in local AGN. First, they confirm that the majority of the *Swift*/BAT catalogue AGN are accreting at low Eddington ratios (Winter et al. 2009) across the range of available absorption properties probed. This result is not significantly modified by possible overestimates of

the black hole mass using our $M_{\rm BH}-L_{\rm bulge}$ approach, as discussed in detail in Vasudevan et al. (2009), since if we calibrate this approach against reverberation mapping as done in their paper we obtain an offset of a factor of $\sim$2, which would shift the Eddington ratios obtained here to correspondingly higher values. However, the centre of the distribution would still be located at low values. At any rate, there are geometrical uncertainties in reverberation mapping which give rise to a tolerance of a factor of $\sim$3 in calibrating the mass estimates.

However, we note the presence of five AGN for which the Eddington ratios could be uncertain because of their mass estimates. Vasudevan et al. (2009) use the 2MASS PSC flux as an estimate of the total unresolved nuclear and bulge light, and calculate the fraction of the 2MASS PSC flux which can be attributed to the bulge. Inspection of the 2MASS images for all of the nearby galaxies reveal that there may be a few sources for which the assumption of an unresolved bulge is not valid, and (apart from the case of Cyg A already discussed) those overlapping with our sample are NGC 6300, NGC 3227, NGC 5728, NGC 7582 and NGC 1365. If the bulge luminosity has been underestimated in these sources, the small resultant black hole masses will artificially increase their Eddington ratios. If corrected, this should shift the average Eddington ratio down for this subsample.

We note that the bolometric luminosities are not dependent on the mass in the simple approach used here, in contrast to the method outlined in Vasudevan & Fabian (2007) and their subsequent studies, which involves fitting a multicolour accretion disc model to optical–UV data with the model normalization constrained by the black hole mass. In the zeroth-order approach presented here, the main uncertainties in determining $L_{\rm bol}$ are the accuracy of the correction for non-nuclear contamination, the accuracy of the nuclear IR SED templates used and the degree of hard X-ray variability (Pozzi et al. 2007 find that using various different IR SED templates does not significantly alter the extrapolated bolometric luminosity, however). As a result, uncertainties in mass estimates only affect Eddington ratios, not bolometric luminosities.

Bolometric corrections are generally lower than those obtained for high-Eddington-rate sources (Vasudevan & Fabian 2009, 2007) and quasars (Elvis et al. 1994). These results provide a very interesting window on to the properties of the more complex high-absorption AGN, as hinted at previously by Pozzi et al. (2007). Our approach aims to by-pass the unwanted complexities introduced by absorption in the optical-to-X-ray regime by using the reprocessed IR and (relatively) unaffected hard X-ray BAT data. Indications of predominantly low bolometric corrections for high-absorption AGN have consequences for matching the local SMBH mass density with that inferred from the X-ray background. A significant population of highly absorbed AGN is required to fit the X-ray background spectrum (Gandhi & Fabian 2003; Gilli et al. 2007), and as discussed in Fabian (2004) bolometric corrections of around $\sim$10– 20 are appropriate for reconciling the XRB with the local black hole mass density.

5.1 Anisotropy and geometry corrections: smooth-versus-clumpy tori

The similar regions of the $L_{12\,\mu\rm m}-L_{2-10\,\rm keV}$ plot in Fig. 4 occupied by both obscured and unobscured sources suggest that the 12 μm luminosities are isotropic (assuming that the absorption responsible for producing the MIR emission is broadly correlated with the X-ray absorption; see Sections 1 and 3.2.3). The SED models and anisotropy corrections used here in calculating $L_{\rm bol}$ are based ultimately on the models of Granato & Danese (1994) which assume a smooth dust distribution in the torus. If the torus is clumpy however, as recent models and fits to the data suggest (Jaffe et al. 2004; Tristram et al. 2007; Beckert et al. 2008), the torus emission is more isotropic and would not require significant anisotropy corrections between edge-on (obscured) and face-on (unobscured) AGN; this is possibly supported by the emergence of a unified $L_{12\,\mu\rm m}-L_{2-10\,\rm keV}$ correlation for both types of AGN and its implication of isotropic MIR emission. If we also inspect the values of 25 μm luminosity plotted against X-ray luminosity, we again find that obscured and unobscured objects do not occupy different regions of the plot, implying that the 25 μm luminosity may also be, to a large degree, isotropic. In any case, even if we remove the isotropy corrections for obscured objects, this would have the effect of reducing bolometric corrections and Eddington ratios further by around 20–30 per cent for that subsample {since $\kappa_{2-10\rm keV} = [L_{\rm X,total} + f_{\rm geo} f_{\rm anisotropy} f_{\rm starlight} L_{\rm IR}^{\rm (nuc,obs)}]/L_{2-10\,\rm keV}$, for geometry, anisotropy and starlight correction factors $f_{\rm geo}$, $f_{\rm anisotropy}$, $f_{\rm starlight}$ discussed previously}. Such a modification would not significantly alter our conclusions.

5.2 Objects not detected by *IRAS*

The non-detection of a substantial fraction of the sample warrants consideration of the expected distribution of values for $\kappa_{2-10\,\rm keV}$ and $\lambda_{\rm Edd}$ from the non-detected objects. Assuming the missing objects are just below detection, the upper limits presented in Fig. 16 imply that the majority of the missing objects would have a very similar distribution of $L_{12\,\mu\rm m}$ values to the detected objects. If the upper limits lie significantly above the relation in comparison to the detected sample, one would expect to see higher bolometric corrections on average due to a bigger potential nuclear IR contribution, and vice versa if they lie significantly below the line. Given that the upper limits also occupy a similar range in $L_{2-10\,\rm keV}$ as the detected sample, the distribution of bolometric corrections would also be expected to be similar. The mean black hole mass for the non-detected sample is $\log(M_{\rm BH}/{\rm M}_\odot) = 7.82$ compared to 7.76 for the detected sample, with very similar spreads, implying that the non-detections may lie at similar Eddington ratios as well. However, this is

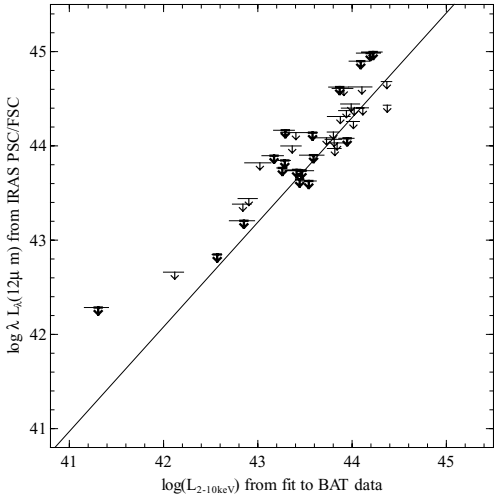

Figure 16. Upper-limiting IR 12 μm luminosity against 2–10 keV luminosity from fits to BAT data, for objects without *IRAS* PSC or FSC data. The completeness limit of the *IRAS* FSC, 0.2 Jansky has been used in calculation of these upper limits.

obviously conjecture, and future work using IR data probing to lower fluxes would be able to verify or challenge these predictions.

6 SUMMARY AND CONCLUSIONS

We have presented a simple extension of the Pozzi et al. (2007) method for calculating the bolometric output of AGN using reprocessed IR emission from *IRAS* along with the hard X-ray emission from *Swift*–BAT. We estimate the integrated nuclear IR luminosity by fitting of AGN nuclear SED templates from Silva et al. (2004) to the IR data, and estimate non-nuclear contamination in the large-aperture *IRAS* fluxes via two methods: the first involves applying a correction to make the distribution of 12 μm fluxes lie on the most recent determination of the $L_{\rm X}-L_{12\,\mu{\rm m}}$ relation determined by Gandhi et al. (2009) and the second involves fitting a host galaxy SED template alongside the nuclear SED template. The second method has the advantage that it does not presuppose a relation between X-ray and MIR luminosity, which will tend to bias the bolometric corrections to certain values, whereas the former method is superior in that it ought to give clean estimates of the core powers alone, on average. We fit a simple power-law model to the hard X-ray BAT data to determine the X-ray luminosities, and then calculate the bolometric luminosity after applying corrections for torus geometry and anisotropy of emission as discussed by Pozzi et al. (2007). We calculate Eddington ratios using black hole masses estimated from the *K*-band bulge luminosity as described in Vasudevan et al. (2009) (and use a well-constrained dynamical mass for the known cD galaxy Cyg A), and present the 2–10 keV bolometric corrections. We calibrate our approach against the simultaneous optical-to-X-ray SEDs from Vasudevan et al. (2009) and find trends for agreement between the two approaches, although there are still numerous sources of scatter.

Using our zeroth-order IR and hard X-ray approach, bolometric corrections for the low-absorption subsample give an average of around ∼22, intermediate between the averages found from the two approaches of removing the host galaxy contamination (19,24). Eddington ratios are ∼0.037 on average, from the two methods. For the high-absorption subsample, the average Eddington ratios are 0.034 and 0.043 from the statistical and host-SED fitting methods for host galaxy removal, respectively. The spread in bolometric corrections is greater than for low-absorption objects, but for the lower part of the Eddington ratio distribution ($\lambda_{\rm Edd} < 0.03$) bolometric corrections are consistently low in both methods for host galaxy contamination removal (∼15). The errors on these average bolometric corrections are typically less than ± ∼3. Using the SED fitting method for host galaxy removal, for $0.03 < \lambda_{\rm Edd} < 0.2$ the high-absorption objects have bolometric corrections of ∼32 ± 10, possibly representing part of the transitional region from low-to-high bolometric corrections near Eddington ratios of ∼0.1 proposed by Vasudevan & Fabian (2007,2009), but better constraints on the host galaxy contamination and black hole masses are needed before this can be established. These bolometric corrections for our local, high-absorption AGN represent a new angle on uncovering the accretion processes at work in this important class of object. The objects not detected by *IRAS* (∼30 per cent of the potential sample) are expected to show similar results based on considerations of their upper limiting IR luminosities, but more sensitive IR observations are needed to confirm this.

These preliminary suggestions that the majority of both high- and low-absorption *IRAS*-detected objects in the *Swift*–BAT catalogue are at low Eddington ratios and exhibit low bolometric corrections reinforces unified scenarios in which the processes at work in AGN of different absorption levels are fundamentally similar, but the observed properties vary chiefly based on orientation. The possible discovery of the lower end of an Eddington-ratio-dependent bolometric correction for high-absorption objects would be an interesting aspect of this finding, subject to the uncertainties already discussed.

Recently, Lamastra et al. (2009) have studied the Eddington ratio distribution of Seyfert 2s from the optical perspective, by estimating the optical bolometric correction factor to the [O III] line luminosity. For their sample of higher redshift AGN ($0.3 < z < 0.8$), they find that Seyfert 2s do not accrete close to the Eddington limit and Eddington ratios are ∼0.1 on average. This work reinforces previous findings of predominantly $\lambda_{\rm Edd} < 0.1$ accretion in the low-redshift Universe (e.g. Sun & Malkan 1989): here, we extend this to an absorption-unbiased sample.

High-absorption objects are the dominant component of the X-ray background, and the identification of predominantly low bolometric corrections for them, using a larger sample than in Pozzi et al. (2007), tells us how accretion on to black holes in the past can account for the current population of dormant massive black holes (as outlined by Soltan 1982 and later authors). Lower bolometric corrections for low accretion rates found here are appropriate for matching the X-ray background energy density to the local black hole mass density (Fabian 2004).

Additionally, the distribution of bolometric corrections in Pozzi et al. (2007) (35 ± 9) is similar to the one we obtain for $0.03 < \lambda_{\rm Edd} < 0.2$ sources (using method 2 for host galaxy correction); indeed, the Eddington ratios in the Pozzi et al. sample also lie predominantly in this range. Our extension of their method down to Eddington ratios as low as $\sim 6 \times 10^{-3}$ for a representative sample of local obscured Seyferts is therefore valuable.

This study is an extension of the Pozzi et al. technique of using the IR and hard X-rays (14–195 keV) for estimating the bolometric output in a way that is less prone to the spectral complexities which affect the optical–UV and X-ray regimes, particularly for obscured objects. However, as discussed at length, appropriate correction for the host galaxy contamination in the IR is essential. A useful extension of this study would be to use higher resolution *Spitzer* data in combination with BAT data to perform the same calculation, which would provide a more accurate measure of the nuclear reprocessed IR without having to apply the large contamination corrections needed here (e.g. Meléndez et al. 2008). The uncertainties in the covering fraction also represent a limitation of the study, and future work determining the appropriate distribution of covering fractions to use will be very valuable.

Some of the uncertainties in the black hole mass estimates should be addressed in the analyses of Winter et al. and Koss et al. (in preparation) which will provide Hβ linewidth-based estimates of the black hole masses in the catalogue, which can be used to refine the position of the sources on the Eddington ratio axis.

One class of object for which our approach may not be appropriate is the Ultraluminous Infrared Galaxy (ULIRG) class. In these, the MIR continuum is not directly attributable to the AGN (e.g. Alonso-Herrero et al. 2006) and so they should be corrected for or excluded when considering the IR continuum of large samples of AGN, as discussed by Thompson et al. (2009). However, the redshift distribution of ULIRGs significantly differs from the BAT catalogue, so we expect contamination to be minimal, with none of the objects presented in our study being classified as ULIRGs in NED.

Questions remain as to exactly what the IR continuum due to reprocessing in AGN is. The continuum produced depends on the dust distribution, grain size and torus geometry; in particular, the

clumpiness or smoothness of the dust distribution is important. Another useful extension to this work would be to explore how different continuum models, for example those for clumpy tori (Hönig et al. 2006; Nenkova et al. 2008a, b), would alter the values of $L_{\rm bol}$ found here, especially as recent observational evidence strongly favours the clumpy torus scenario. The recent work of Ramos Almeida et al. (2009), who fit clumpy torus models to mid-IR SEDs for a small sample of AGN, paves the way for further studies in this area.

The 9-month BAT catalogue (Tueller et al. 2008) has provided numerous opportunities to understand the accretion processes at work in local AGN (e.g. Mushotzky et al. 2008; Vasudevan et al. 2009; Winter et al. 2009). Similar follow-up studies on the recently released 22-month BAT catalogue will afford the chance to widen these analyses to a larger, more representative sample of local AGN.

ACKNOWLEDGMENTS

RVV acknowledges support from the Science and Technology Facilities Council, ACF thanks the Royal Society for Support and PG acknowledges a RIKEN Foreign Postdoctoral Research fellowship. We thank the *Swift*/BAT team for the 9-month AGN catalogue BAT data. We thank Richard McMahon for help with processing and understanding the *IRAS* data. We thank Laura Silva for providing us with the SED templates and clarifying related issues. We also thank the anonymous referee for helpful comments and suggestions that improved this paper. This research has made use of the NED and the NASA/IPAC Infrared Science Archive, which are operated by the Jet Propulsion Laboratory, California Institute of Technology, under contract with the National Aeronautics and Space Administration.

REFERENCES

Alonso-Herrero A. et al., 2006, ApJ, 640, 167
Antonucci R., 1993, ARA&A, 31, 473
Awaki H. et al., 2008, PASJ, 60, 293
Barvainis R., 1987, ApJ, 320, 537
Beckert T., Driebe T., Hönig S. F., Weigelt G., 2008, A&A, 486, L17
Brocksopp C., Starling R. L. C., Schady P., Mason K. O., Romero-Colmenero E., Puchnarewicz E. M., 2006, MNRAS, 366, 953
Elvis M. et al., 1994, ApJS, 95, 1
Fabian A. C., 2004, in Ho L. C., ed., Coevolution of Black Holes and Galaxies. Cambridge Univ. Press, Cambridge, p. 446
Gandhi P., Fabian A. C., 2003, MNRAS, 339, 1095
Gandhi P., Horst H., Smette A., Hönig S., Comastri A., Gilli R., Vignali C., Duschl W., 2009, A&A, 502, 457
Garcet O. et al., 2007, A&A, 474, 473
Gilli R., Comastri A., Hasinger G., 2007, A&A, 463, 79
Granato G. L., Danese L., 1994, MNRAS, 268, 235
Hönig S. F., Beckert T., Ohnaka K., Weigelt G., 2006, A&A, 452, 459
Horst H., Smette A., Gandhi P., Duschl W. J., 2006, A&A, 457, L17
Horst H., Gandhi P., Smette A., Duschl W. J., 2008, A&A, 479, 389
Ikeda S., Awaki H., Terashima Y., 2009, ApJ, 692, 608
Iwasawa K., Koyama K., Awaki H., Kunieda H., Makishima K., Tsuru T., Ohashi T., Nakai N., 1993, ApJ, 409, 155
Jaffe W. et al., 2004, Nat, 429, 47
Lamastra A., Bianchi S., Matt G., Perola G. C., Barcons X., Carrera F. J., 2009, A&A, 504, 73
McKernan B., Ford K. E. S., Chang N., Reynolds C. S., 2009, MNRAS, 394, 491
Maiolino R., Risaliti G., 2007, in Ho L. C., Wang J.-W., eds, ASP Conf. Ser. Vol. 373, The Central Engine of Active Galactic Nuclei. Astron. Soc. Pac., San Francisco, p. 447
Marconi A., Hunt L. K., 2003, ApJ, 589, L21
Mateos S., Barcons X., Carrera F. J., Ceballos M. T., Hasinger G., Lehmann I., Fabian A. C., Streblyanska A., 2005, A&A, 444, 79
Meléndez M., Kraemer S. B., Schmitt H. R., Crenshaw D. M., Deo R. P., Mushotzky R. F., Bruhweiler F. C., 2008, ApJ, 689, 95
Miniutti G. et al., 2007, PASJ, 59, 315
Mushotzky R., 2004, in Barger A. J., ed., Astrophysics and Space Science Library, Vol. 308, Supermassive Black Holes in the Distant Universe. Kluwer, Dordrecht, p. 53
Mushotzky R. F., Winter L. M., McIntosh D. H., Tueller J., 2008, preprint (arXiv:0807.4695)
Nenkova M., Sirocky M. M., Ivezić Ž., Elitzur M., 2008a, ApJ, 685, 147
Nenkova M., Sirocky M. M., Nikutta R., Ivezić Ž., Elitzur M., 2008b, ApJ, 685, 160
Pier E. A., Krolik J. H., 1992, ApJ, 401, 99
Pozzi F. et al., 2007, A&A, 468, 603
Ramos Almeida C. et al., 2009, ApJ, 702, 1127
Risaliti G. et al., 2009, ApJ, 696, 160
Rowan-Robinson M., Valtchanov I., Nandra K., 2009, MNRAS, 397, 1326
Shields G. A., 1978, Nat, 272, 706
Silva L., Maiolino R., Granato G. L., 2004, MNRAS, 355, 973
Silverman J. D. et al., 2005, ApJ, 618, 123
Soltan A., 1982, MNRAS, 200, 115
Strateva I. V., Komossa S., 2009, preprint (arXiv:0903.1548)
Sun W.-H., Malkan M. A., 1989, ApJ, 346, 68
Tadhunter C., Marconi A., Axon D., Wills K., Robinson T. G., Jackson N., 2003, MNRAS, 342, 861
Thompson G. D., Levenson N. A., Uddin S. A., Sirocky M. M., 2009, ApJ, 697, 182
Tristram K. R. W. et al., 2007, A&A, 474, 837
Tueller J., Mushotzky R. F., Barthelmy S., Cannizzo J. K., Gehrels N., Markwardt C. B., Skinner G. K., Winter L. M., 2008, ApJ, 681, 113
Tully R. B., 1994, Nearby Galaxies Catalogue, VizieR Online Data Catalog, 7145
Vasudevan R. V., Fabian A. C., 2007, MNRAS, 381, 1235
Vasudevan R. V., Fabian A. C., 2009, MNRAS, 392, 1124
Vasudevan R. V., Mushotzky R. F., Winter L. M., Fabian A. C., 2009, MNRAS, 399, 1553
Vaughan S., Fabian A. C., 2004, MNRAS, 348, 1415
Winter L. M., Mushotzky R. F., Reynolds C. S., Tueller J., 2009, ApJ, 690, 1322
Zdziarski A. A., Ghisellini G., George I. M., Fabian A. C., Svensson R., Done C., 1990, ApJ, 363, L1

This paper has been typeset from a TEX/LATEX file prepared by the author.